THE JOURNAL OF PHYSICAL CHEMISTRY B
A JOURNAL OF THE AMERICAN CHEMICAL SOCIETY

pubs.acs.org/JPCB
Article

Thermodynamics and *S*-Palmitoylation Dependence of Interactions between Human Aquaporin-4 M1 Tetramers in Model Membranes

Jessica D. Carder, Barbara Barile, Krista A. Shisler, Francesco Pisani, Antonio Frigeri, K. W. Hipps, Grazia Paola Nicchia,* and James A. Brozik*

Cite This: *J. Phys. Chem. B* 2024, 128, 603−621
Read Online

ACCESS | Metrics & More | Article Recommendations | Supporting Information

ABSTRACT: Aquaporin-4 (AQP4) is a water channel protein found primarily in the central nervous system (CNS) that helps to regulate water−ion homeostasis. AQP4 exists in two major isoforms: M1 and M23. While both isoforms have a homotetrameric quaternary structure and are functionally identical when transporting water, the M23 isoform forms large protein aggregates known as orthogonal arrays of particles (OAPs). In contrast, the M1 isoform creates a peripheral layer around the outside of these OAPs, suggesting a thermodynamically stable interaction between the two. Structurally, the M1 isoform has an N-terminal tail that is 22 amino acids longer than the M23 isoform and contains two solvent-accessible cysteines available for *S*-palmitoylation at cysteine-13 (Cys-13) and cysteine-17 (Cys-17) in the amino acid sequence. Earlier work suggests that the palmitoylation of these cysteines might aid in regulating AQP4 assemblies. This work discusses the thermodynamic driving forces for M1 protein−protein interactions and how the palmitoylation state of M1 affects them. Using temperature-dependent single-particle tracking, the standard state free energies, enthalpies, and entropies were measured for these interactions. Furthermore, we present a binding model based on measured thermodynamics and a structural modeling study. The results of this study demonstrate that the M1 isoform will associate with itself according to the following expressions: $2[\text{AQP4-M1}]_4 \leftrightarrow [[\text{AQP4-M1}]_4]_2$ when palmitoylated and $3[\text{AQP4-M1}]_4 \leftrightarrow [\text{AQP4-M1}]_4 + [[\text{AQP4-M1}]_4]_2 \leftrightarrow [[\text{AQP4-M1}]_4]_3$ when depalmitoylated. This is primarily due to a conformational change induced by adding the palmitic acid groups at Cys-13 and Cys-17 in the N-terminal tails of the homotetramers. In addition, a statistical mechanical model was developed to estimate the Gibbs free energy, enthalpy, and entropy for forming dimers and trimers. These results were in good agreement with experimental values.

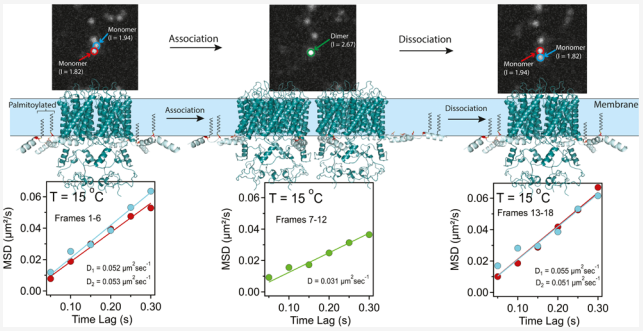

1. INTRODUCTION

Aquaporin-4 (AQP4) is one of the most abundant water channels in the central nervous system (CNS), mainly concentrated in the end feet of astrocytes at the interfaces between cerebrospinal fluid and CNS vasculature.[1] AQP4 maintains water−ion homeostasis in the brain, facilitating fast water transport through cellular membranes.[2] The dysregulation of AQP4 leads to aberrant subcellular localization and aggregation properties as seen in various neurogenic conditions, including but not limited to Alzheimer's disease, stroke, and Neuromyelitis Optica (NMO) spectrum disorder, which causes damage to optic nerves due to excessive inflammation.[3−6] Insights into the fundamental chemistry behind AQP4 behavior are imperative for understanding the progression of these neurological diseases.

AQP4 is a tetrameric protein with eight hydrophobic membrane domains connected by joining loops, an intracellular N-terminal domain, and an intracellular C-terminal domain.[7] AQP4 comes in two major isoforms: M1, known as the long form, which initiates at the methionine 1 residue, and M23, known as the short form, which initiates at the methionine 23 residue. The N-terminal domain of M1 is 31 amino acids long and the N-terminal domain of M23 is only 9 amino acids long. The C-terminal domain of both isoforms is much larger at 73 amino acids long or 102 amino acids long for the extended form (AQP4_{ext}).[8−10] The M1 isoform also contains two solvent-accessible cysteines on the N-terminal chain that the M23 isoform does not have, making it a candidate for post-translational modifications.[11] Both isoforms of AQP4 are found in the CNS in varying ratios, but it is commonly seen that the M23 isoform is three times more abundant than the M1 isoform in cellular membranes.[12]

Received: July 5, 2023
Revised: December 9, 2023
Accepted: December 21, 2023
Published: January 12, 2024

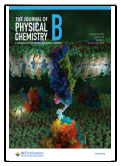

Functionally, both isoforms can transport water; the key difference is how they are stabilized in the plasma membrane.

In cellular membranes, M23 forms large protein aggregates known as orthogonal arrays of particles (OAPs), composed of up to 50 or more discrete tetrameric units.[13−15] The M1 isoform does not assemble into OAPs; instead, it forms a peripheral coating around the M23-OAPs, effectively capping the OAP to a specific size.[16−18] This phenomenon has been seen extensively using super-resolution fluorescence and electron microscopy. The interactions between the M1 and M23 isoforms in these OAPs have been well studied; however, the interactions between the M1 isoforms have yet to be extensively characterized.

As previously mentioned, the M1 isoform contains two cysteines on the N-terminus (Cys-13 and Cys-17) that the M23 isoform does not have. *S*-Palmitoylation is an enzymatic post-translational modification that attaches palmitic acid to a cysteine residue through a thioester linkage. It is well known that *S*-palmitoylation plays a pivotal role in protein regulation, including the promotion of membrane affinity, changes in the steric configuration of proteins, and the regulation of protein trafficking, among other functions.[19−23] It has been previously shown, using AQP4-M1 mutants that had segments of the N-terminus removed, that the palmitoylation sites on the N-terminus directly affect the ability of M1 to form OAPs. These studies proposed *S*-palmitoylation as a possible regulation mechanism for AQP4 OAP growth.[24]

The supramolecular structure of AQP4-M23 is known, and the binding conformations of the individual protein subunits have been determined. It has been shown that AQP4-M23 forms OAPs that are slightly offset on the corners. Each tetramer parallels the other, with two hydrogen binding interactions between the Tyr250 and the Arg108 residues at the interface between two adjacent AQP4-M23s.[25−27] The disorder on the N-terminal chain makes it difficult to characterize with electron microscopy or X-ray diffraction, leaving the binding interactions between adjacent M1 isoforms unresolved.

The fundamental unit of an AQP4-M1 is a highly stable homotetramer $[AQP4\text{-}M1]_4$ with four equal sides and rounded corners (top view). This study shows that, in lipid bilayers, there is an equilibrium between fundamental AQP4-M1 units given by the following equilibrium expressions: $2[AQP4\text{-}M1]_4 \leftrightarrow [[AQP4\text{-}M1]_4]_2$ when palmitoylated and $3[AQP4\text{-}M1]_4 \leftrightarrow [AQP4\text{-}M1]_4 + [[AQP4\text{-}M1]_4]_2 \leftrightarrow [[AQP4\text{-}M1]_4]_3$ when depalmitoylated. For simplicity, we have adopted the following language: $[AQP4\text{-}M1]_4 \equiv$ monomer; $[[AQP4\text{-}M1]_4]_2 \equiv$ dimer; $[[AQP4\text{-}M1]_4]_3 \equiv$ trimer. Presented are the results of a temperature-dependent single-protein tracking study, using time-lapse single-molecule fluorescence microscopy, in which the equilibrium distribution is directly observed. From those observations, the thermodynamic driving forces, K_{eq}, $\Delta G°$, $\Delta H°$, and $\Delta S°$, of dimer and trimer formation were extracted. This was carried out on fully palmitoylated, chemically depalmitoylated, and chemically repalmitoylated samples. In addition to the experimentally measured thermodynamic driving forces, a simple statistical mechanical model is presented that corresponds well to dimer and trimer formation.

2. MATERIALS AND METHODS

2.1. Materials. Water was purified from deionized water using a Barnstead Nanopure filtration system to remove trace organic contaminants and ions down to 18.3 mΩ resistance (purified water). All lipids were purchased from Avanti Polar Lipids (Alabaster, AL). *N*-ethylmaleimide (NEM) was purchased from Chem-Impex (Wood Dale, IL), and hydroxylamine (HAM) was purchased from Millipore Sigma (Burlington, MA). Decyl-maleimide was purchased from Sigma-Aldrich (St. Louis, MO). Fluorescent dyes were purchased from ATTO-TEC (Siegen, Germany). Dialysis tubes were purchased from G Biosciences (St. Louis, MO). Protein gels and standards were purchased from Bio-Rad (Hercules, CA), and protein concentrators were purchased from Corning Life Sciences (Durham, NC). All chemicals and lipids were used as received. Materials for cell cultures and protein expression were purchased from Thermo Fisher Scientific (Waltham, MA) or Euroclone (Italy) when specified. Ni^{2+}-NTA Agarose beads were purchased from QIAGEN (Redwood City, CA).

2.2. Cell Cultures. The *Spodoptera frugiperda* Sf9 cells were grown as adherent cultures in Gibco Supplemented Grace's Insect Medium with 5% heat-inactivated fetal bovine serum (FBS), 100 UI/mL penicillin, and 100 mg/mL streptomycin (Euroclone, Italy) in incubators set at 27 °C without CO_2 exchange. Suspension cultures were grown in serum-free Gibco Sf-900II SFM under constant shaking at 120 rpm in a nonhumidified incubator at 27 °C. Adherent cultures were used for primary transfection with recombinant bacmid DNA and suspension cultures for viral amplification and protein expression.

2.3. Expression of hAQP4-M1 in *Spodoptera frugiperda* Sf9 Cells. AQP4-M1 proteins were produced in *Spodoptera frugiperda* (Sf9) cells using the Bac-to-Bac Baculovirus Expression System (Thermo Fisher Scientific, Waltham, MA), as suggested by the manufacturer. The mutant human sequence AQP4-M1M23I with a histidine tag (6xHis) was used for the recombinant tetramer-forming AQP4-M1 isoform due to the evidence of a leaky scanning mechanism in the full-length AQP4 transcript.[28] In the present manuscript, we will refer to hAQP4-M1M23I-6xHis as AQP4-M1. The 6xHis tag is at the C-terminus located on the intracellular side of the protein. Briefly, the AQP4-M1 sequence was cloned into pFastBac donor plasmid flanked by sequences for transposition. MAX Efficiency Competent DH10Bac *Escherichia coli* cells were transformed with the recombinant donor plasmid and positive colonies were screened on LB agar plates containing 50 μg/mL kanamycin, 7 μg/mL gentamicin, and 10 μg/mL tetracycline, 100 μg/mL Bluo-gal, and 40 μg/mL IPTG. The recombinant bacmid DNA was then isolated from transformed colonies using PureLinkHiPure Plasmid DNA Miniprep Kit, analyzed by PCR by using a Platinum Taq DNA Polymerase High Fidelity kit, and used to transfect Sf9 cells by Cellfectin II Reagent and amplify the viral titer. The expanded viral stock was employed to infect insect cells in suspension and induce protein expression.

2.4. Cell Membrane Preparation, Protein Extraction from Membranes, and Purification. ***Cell Membrane Preparation***: 72 h post viral transfection, cells were harvested at 500*g* for 6 min. The pellet was resuspended in 10 volumes of 20 mM Tris-HCl pH 7.5 + Protease Inhibitor (PI) and homogenized with a Dounce homogenizer on ice. The sample was centrifuged at 800*g* for 10 min, then the supernatant was collected and centrifuged at 100,000*g* for 60 min at 4 °C (Beckman Centrifuge, 70Ti). The pellet was resuspended in 10 volumes of 20 mM Tris-HCl pH 7.5 + Protease Inhibitor (PI) buffer and centrifuged at 100,000*g* for 60 min at 4 °C. This

https://doi.org/10.1021/acs.jpcb.3c04529
J. Phys. Chem. B 2024, 128, 603−621

Scheme 1. Synthetic Scheme Used to Chemically Modify AQP4-M1[a]

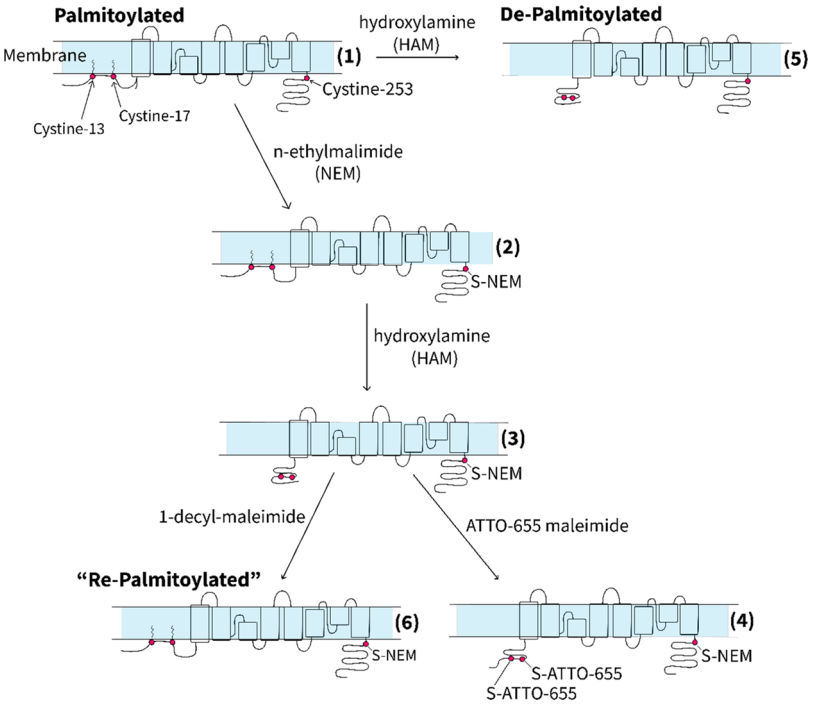

[a](1) is M1P, (5) is M1D, and (6) is M1R.

step was performed two times. ***Protein Extraction from Membranes:*** The resultant pellet was then resuspended in 10 volumes of solubilization buffer (2% DDM, 300 mM NaCl, 10% Glycerol, 5 mM Imidazole pH = 7 + PI), vortexed every 5 min for 1 h, then centrifuged at 17,000*g* for 30 min at 4 °C. The supernatant was then collected and purified. ***Protein Purification:*** Protein purification was performed by nickel-based chromatography. Briefly, Ni^{2+}-NTA Agarose beads were thoroughly resuspended and washed four times. Protein samples were then incubated with the beads on a nutator at 4 °C overnight. The next day, samples were centrifuged at 1000*g* for 1 min to pellet the beads and discard the supernatant (flow-through). Beads were washed in 5 volumes of washing buffer (2% DDM, 300 mM NaCl, 10% Glycerol, 20 mM Imidazole pH = 7), nutated for 15 min at 4 °C on a rotary shaker and centrifuged at 1000*g* for 1 min. This step was repeated seven times to discard the supernatant and thoroughly rinse the beads. After the final wash, the beads were incubated with two volumes of elution buffer (2% DDM, 300 mM NaCl, 10% Glycerol, 250 mM Imidazole) with protease inhibitor and nutated for 5 min at 4 °C. Samples were then centrifuged at 1000*g* for 1 min. The supernatant was collected and stored as the final eluted sample. Three eluted samples were obtained, dialyzed in HBS buffer, and stored at −80 °C until ready for use. Protein expression was checked by sodium dodecyl sulfate polyacrylamide gel electrophoresis (SDS-PAGE) and Coomassie G-250 staining, revealed by Western Blot by anti-AQP4 antibody (Sigma-Aldrich, A5971), and quantified using the Micro-BCA Protein Assay Kit (Thermo Fisher Scientific, Waltham, MA), as previously described.[29]

2.5. Degree of *S*-Palmitoylation. The degree of palmitoylation for AQP4-M1 expressed in Sf9 cells was determined using a modified, published protocol by Green and co-workers (depicted in Scheme 1).[30] The first step was to protect nonpalmitoylated solvent-exposed cysteines by reacting AQP4-M1 with a 50-molar excess of *N*-ethylmaleimide (NEM) from a 10 mM solution (in HEPES buffered saline (HBS buffer)) mixing the solution on a nutator at 4 °C overnight to afford (**2**) in Scheme 1. The excess NEM was removed by overnight dialysis against HBS buffer (pH = 7.4). Next, all palmitic acid groups covalently bound to any cysteine residue in AQP4-M1 were cleaved using a 1 M hydroxylamine (HAM) solution (1:1 by volume of AQP4/HAM) and mixed on a nutator at 4 °C overnight before dialysis against fresh HBS buffer to remove excess HAM from the solution to afford (**3**) in Scheme 1. Finally, (**3**) was reacted with a 3.2 molar excess of ATTO-655 maleimide and mixed on a nutator at 4 °C for ∼12 h before overnight dialysis against HBS buffer to remove any excess dye and afford (**4**) in Scheme 1. Note: the 3.2 molar excess was calculated per AQP4-M1 subunit forming the aquaporin tetramer. The degree of labeling (DOL) was then determined with an ND-1000 NanoDrop spectrometer using the analysis protocol supplied by the manufacturer.[31] Since the only cysteines available for labeling are those made available by the HAM cleavage, the degree of labeling is equal to the degree of palmitoylation (DOP).

2.6. Depalmitoylation and "Re"-Palmitoylation. Purified AQP4-M1 was depalmitoylated similarly as described above except for NEM protection (see Scheme 1; depalmitoylated (**5**)). Depalmitoylated AQP4-M1 was prepared by treatment of AQP4-M1 with a 1 M HAM solution (1:1 by volume M1/HAM) and allowed to mix overnight on a nutator at 4 °C. After cleavage of the *S*-palmitoylation groups, excess HAM was removed by overnight dialysis against fresh HBS buffer at 4 °C. To ensure depalmitoylated AQP4-M1 was still present and not degraded, the sample in the HBS buffer was concentrated to a working concentration to run an SDS page gel using a Corning 10 kDa cutoff protein spin concentrator (working concentration = 2.4 μM, volume loaded on gel = 7.5

https://doi.org/10.1021/acs.jpcb.3c04529
J. Phys. Chem. B 2024, 128, 603−621

μL). The gel was run on a Bio-Rad Mini-PROTEAN TGX precast gel (4−15%) using the Bio-Rad Precision Plus Protein Standards reference ladder (see Figure S1 in the Supporting Information).

Samples were also prepared where AQP4-M1 was first depalmitoylated and later chemically "repalmitoylated" by attaching a long alkane chain to Cys-13 and Cys-17 to make certain that any physical changes seen in depalmitoylated samples could be reversed. To do this, the NEM-protected product (**2**) in Scheme 1 was treated with a 3.2 molar excess of 1-decyl-maleimide at 4 °C overnight. The excess 1-decyl-maleimide was then removed by dialysis against fresh HBS buffer to afford the repalmitoylated sample (**6**) in Scheme 1. Note that the decyl-carbon chain is 6 carbons shorter than the natural palmitic acid. We have retained the "repalmitoylation" nomenclature to reinforce the logic of re-adding two lipid tails to the N-terminal chain of the AQP4 after they had been removed previously. Repalmitoylated AQP4-M1 was also subjected to SDS page electrophoresis to ensure the protein was present and not degraded, as described above (see Figure S1; Supporting Information).

2.7. Protein Labeling. The protein was labeled directly per the manufacturer's instructions for single-molecule experiments. In an Eppendorf tube, the protein was mixed with ATTO 647N NHS-Ester in 2× molar excess (per subunit) and mix at 4 °C overnight. The labeled protein was then transferred to a dialysis tube and dialyzed against HBS buffer to remove any excess dye. The degree of labeling (DOL) was then determined with an ND-1000 NanoDrop spectrometer using the analysis protocol supplied by the manufacturer.[31] The DOL per AQP4 tetramer was 4.12 (∼1 per subunit in the homotetramer).

2.8. Liposome Formation. Liposomes were composed of 98.6% 1-palmitoyl-2-oleoyl-glycerol-3-phosphocholine (POPC) and 1.4% 1,2-stearoyl-*sn*-glycerol-3-phosphoethanolamine-N-[methoxy(polyethylene glycol)-2000] (ammonium salt) (PEG−PE). Liposomes were prepared as previously described.[32−34] Briefly, liposomes were prepared from lipid cakes made by evaporating 1 mL of a 9:1 chloroform: methanol solution that contained the above-outlined lipid mixtures. The solution was then evaporated overnight under a stream of prepurified nitrogen until no chloroform or methanol remained, and the lipid cake was thoroughly dry. The cake was then rehydrated in HBS buffer by heating it in a 60 °C water bath for 1 h with occasional stirring. The solution was then sonicated for 45 min to form small unilamellar vesicles (SUVs). The solution was then removed from the bath, placed in an Eppendorf tube, and centrifuged at 30,000*g* for 2 h to remove any aggregated lipids not incorporated into SUVs. The SUVs were then stored at room temperature and used within 1 week, or aliquoted and flash-frozen in liquid nitrogen and stored at −80 °C.

2.9. Supported Lipid Bilayers. Supported lipid bilayers were prepared as previously described.[35] Briefly, supported bilayers were formed by adding liposomes to hydrophilically treated quartz coverslips. The coverslips were heated at 80 °C for 30 min in a 1:1:1 by volume solution of water, nitric acid, and 30% hydrogen peroxide, and then stored in purified water and used the same day. To prepare a lipid bilayer, a coverslip was removed from the storage water and dried with prepurified nitrogen. The coverslip was then placed into a custom-milled sample holder and fitted with an 8 mm parafilm gasket. 50 μL of SUVs were then pipetted into the center of the parafilm gasket and incubated for 1 h at 37 °C to let the SUVs rupture and form a continuous lipid bilayer. The bilayer was then washed 10 times with the HBS buffer and was ready for use.

2.10. Sample Preparation. To insert the AQP4-M1 proteins into the supported lipid bilayers, the labeled protein was mixed with a Triton X-100 solution in HBS buffer to create a 50 nM protein with 1% detergent solution. The HBS buffer solution above the supported lipid bilayer was then replaced with the detergent plus protein solution and incubated at 37 °C for 1 h. The sample was then gently washed 10 times with detergent-free HBS buffer to remove any protein not incorporated into the bilayer as well as the detergent. Aquaporins that were incorporated into the membrane did so in an irreversible manner. Immediately after the final wash, the sample was mounted on a custom total internal reflection fluorescence microscope (TIRF microscope) and allowed to equilibrate on the temperature-controlled stage at either 20, 25, 30, or 37 °C for 30 min before data collection to ensure thermal equilibrium was reached. Samples were prepared fresh each day. To confirm that the solid-supported lipid bilayer membranes remained intact after treatment with detergent, membranes containing 0.1%, 2-dimyristoyl-*sn*-glycero-3-phosphoethanolamine-*N*-(lissamine rhodamine B sulfonyl) (ammonium salt) (Rhodamine-DMPE) were prepared in the same manner as described above. These solid-supported lipid bilayers were then incubated with 1% Triton X-100 at 37 °C for 1 h and gently washed 10 times with detergent-free HBS. Fluorescence recovery after photobleaching studies were carried out to ensure the membranes remained intact with FRAP recoveries close to that expected for membranes in which the main constituent is POPC (see Figure S2 in the Supporting Information).[36] Detergent-mediated insertion of transmembrane protein into preformed lipid bilayers generally results in unidirectional insertion of the protein.[37,38] AQP4 has both its N- and C- terminal chains on the same side of the bilayer (large hydrophilic domains) and it has been shown that hydrophobic interactions are a major driving force in the insertion of proteins into bilayers.[39] Therefore, it is anticipated that the N- and C- terminal domains will face away from the solid support while the hydrophobic α-helices and joining loops will insert into the membrane. The low degree of immobilization is consistent with the large "intracellular" domain facing away from the solid support (see Section 3.3).

2.11. Temperature-Dependent Single-Protein Tracking. Single-protein tracking studies were performed using a custom TIRF microscope that has been used in previous single-molecule studies.[32] In these experiments, the samples were excited with a 633 nm He:Ne laser. The laser line was first passed through a band-pass filter (633/10X; Chroma Tech.) to clean up the laser line. To avoid polarization effects in the optics train and at the sample, the laser excitation was converted from linearly polarized light to circularly polarized light with a 1/4 waveplate (WPQ05M-633; Thorlabs, Inc.). The beam was then focused with a 200 mm lens onto the back edge of a 100× 1.45 N/A apochromatic TIRF microscope objective (Olympus, Inc.) with a dichroic mirror (FF545/650-Di01; Semrock, Inc.). The beam was positioned along the far edge of the microscope objective using a translation stage so that the angle of the excitation beam was greater than the critical angle between the glass−water interface at the sample. This produced an evanescent field (known as "through

https://doi.org/10.1021/acs.jpcb.3c04529
J. Phys. Chem. B 2024, 128, 603−621

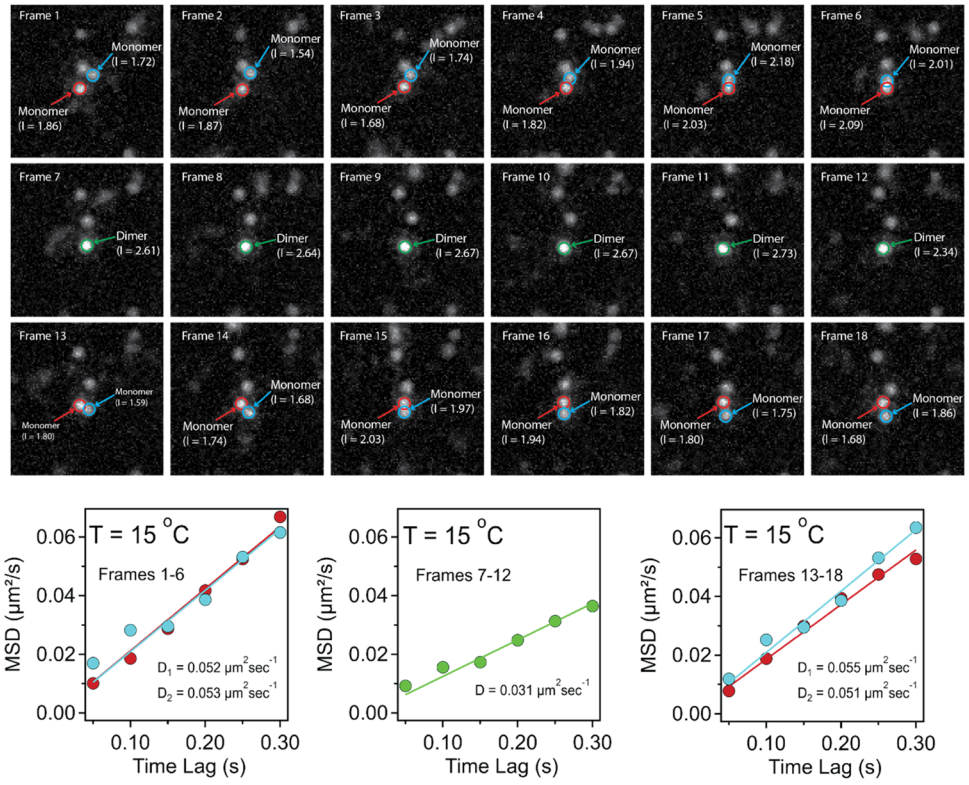

Figure 1. Images are individual frames from a single-particle tracking experiment with M1P at 15 °C. The screenshots begin at frame 1 and end at frame 18. Each frame has a 50 ms exposure. Red and blue circles indicate two particles that have been tracked and identified as monomers. The value for the intensity, I, is the intensity integrated within each circle and in units of grayscale divided by a factor of 10^6 for clarity. The green circle in frames 7−12 is a dimer formed from the monomers depicted by the red and blue circles. The graphs below the images are MSD vs time lag curves for frames 1−6, 7−12, and 13−18, and the lines and markers are color-coded to match the specific particles indicated in the images. The D's are diffusion constants for the individual particles determined from MSD = $4D^*\tau$.

objective total internal reflection fluorescence (TIRF) microscopy").

The emission from fluorescently labeled proteins was then collected by the microscope objective, passed through the dichroic mirror, then a long-pass filter (ET655lp; Chroma Technologies Corp.), and imaged onto an EMCCD camera (iXon 888; Andor Tech.) with a 300 mm achromatic lens. Temperature control was maintained at the sample and the microscope objective with a custom-made sample holder and objective collar. Both were fitted with a Peltier heat pump (TEC3−2.5; Thorlabs, Inc.) and interfaced to separate Meerstetter Engineering temperature controllers (model TEC-1091). The temperature was monitored at the sample with a Pt temperature sensor (TH100PT; Thorlabs, Inc.) and the hot side of the Peltiers with a thermistor (TH10K; Thorlabs, Inc.).

The exposure time for the camera was set to 50 ms and the frame rate was only slightly higher at 50.02 ms. Single-protein tracking analysis was done in MATLAB (MathWorks) using code based on work by Crocker and Grier using scripts modified and previously used by the authors.[33,35,40,41] The vast majority of tracks were greater than 4 frames, with the average track lasting ∼24 frames (∼1.2 s) before photobleaching (recall that there are, on average, 4 fluorophores for each homotetramer). The few tracks that lasted four frames or less were considered too transient to be a transmembrane protein and likely caused by a fluorescent contaminate that reversibly interacted with the membrane. Before the tracking analysis, data sets were first cropped to a uniform size of 150 × 150 pixels and background-corrected using ImageJ's background subtraction function with a 5-pixel sliding paraboloid radius.[42]

2.12. Structure Prediction/Modeling. The predicted structure of human AQP4 was constructed using RoseTTAFold on the Robetta server from the Baker laboratory.[43] The human APQ4M1 sequence was provided to the RoseTTAFold server and five monomer models were generated with a confidence score of 0.7064 (out of 1). This server uses other known structures, such as those in the Protein Data Bank (PDB), and algorithms based on the amino acid sequence, and a neural network to predict structures. The best model from the five predicted structures was selected where the N- and C-terminal regions reside on the intracellular side. This model was then manipulated using PyMol to estimate hypothetical depalmitoylated and palmitoylated states. The two-dimensional (2D) electron crystal structure of rat AQP4[44] was used as a reference for the manipulation of the N-terminal helix−loop−helix region to construct the depalmitoylated and palmitoylated states. In this structure, AQP4 crystallized in a 2D array of repeating AQP4 tetramers.[44] This array was used as the basis for hypothetical dimers and trimers of depalmitoylated and palmitoylated APQ4 and the human model was duplicated in the arrays. The N-terminal regions were rotated along flexible loop regions to accommodate dimer (palmitoylated form) or trimer (depalmitoylated form) formation using PyMol.

https://doi.org/10.1021/acs.jpcb.3c04529
J. Phys. Chem. B 2024, 128, 603−621

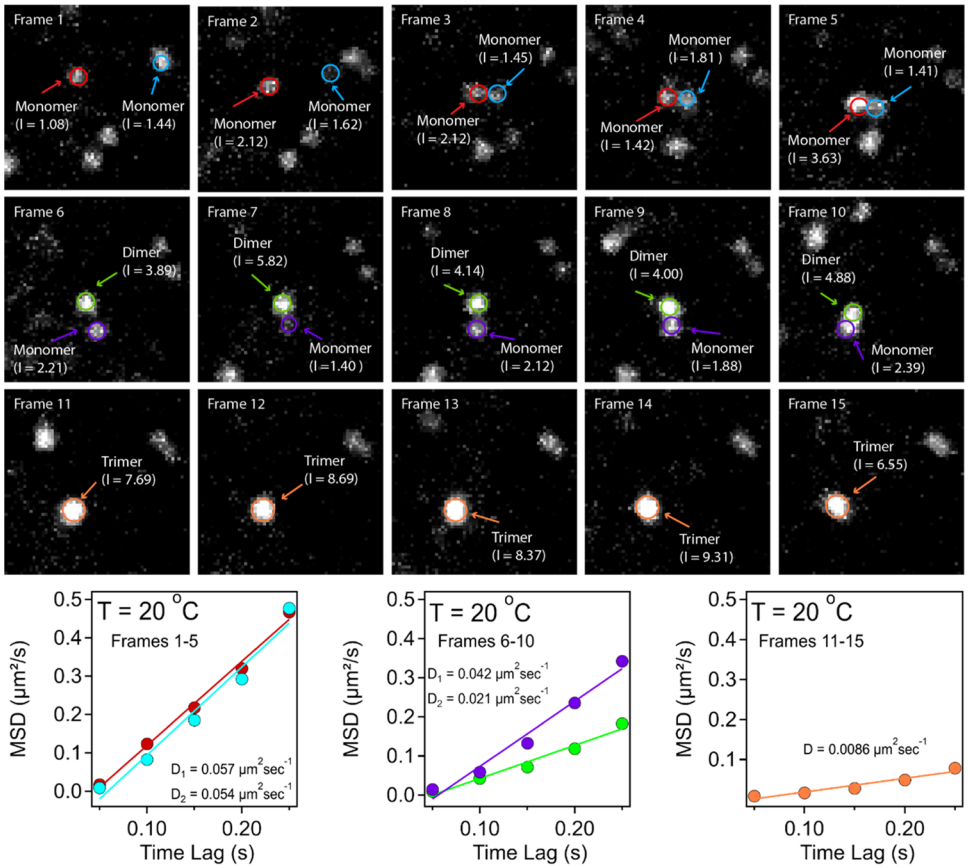

Figure 2. Images are individual frames from a single-particle tracking experiment with M1D at 20 °C. The screenshots begin at frame 1 and end at frame 15. Each frame has a 50 ms exposure. Red and blue circles in frames 1−5 indicate two particles that have been tracked and identified as monomers. In frames 6−10, the green circle is a particle identified as a dimer formed from the monomer depicted by the red and blue circles, and the purple circle is a particle identified as a monomer. In frames 11−15, the particle indicated by the orange circle is identified as a trimer formed from the dimer (green circle) and monomer (purple circle). The value for the intensity, I, is the intensity integrated within each circle and in units of grayscale divided by a factor of 10^6 for clarity. The graphs below the images are MSD vs time lag curves for frames 1−5, 6−10, and 11−15, and the lines and markers are color-coded to match the specific particles indicated in the images. The D's are diffusion constants for the individual particles determined from MSD = $4D^*\tau$.

3. RESULTS

3.1. Nomenclature. Throughout the rest of the article, we will use the following nomenclature, (1) AQP4-M1, (**1**) in Scheme 1, will be referred to as M1P, (2) depalmitoylated AQP4-M1, product (**5**) in Scheme 1, will be referred to as M1D, (3) "repalmitoylated" AQP4-M1, product (**6**) in Scheme 1, will be referred to as M1R, and (4) AQP4-M1 will be a general reference to all aquaporins, regardless of palmitoylation state, in this study.

3.2. Degree of Palmitoylation. Each AQP4-M1 subunit has eight total solvent-accessible cysteines. Moreover, Cys-13 and Cys-17 are possible sites for palmitoylation.[45] Almost every other cysteine is in the hydrophobic transmembrane regions of the AQP4-M1 subunits and are thought to be nonsolvent accessible. The one exception is Cys-253 which is on the C-terminal tail close to the last transmembrane region as indicated in Scheme 1 and may be solvent-accessible. The degree of palmitoylation (DOP) was determined as described in Section 2.5. Using this assay, the DOP was estimated to be 2.09 indicating that both Cys-13 and Cys-17 are palmitoylated (fully palmitoylated) when overexpressed in Sf9 cells. It is noted here that product (**2**) in Scheme 1 was also treated with excess ATTO-655 maleimide, as a control experiment, resulting in no observable fluorescence labeling (DOP = 0 for M1P and M1R). This gives strong evidence that the NEM protection proceeded to completion. If the efficiency of the decyl-maleimide chemistry is similar to that observed for ATTO-655 maleimide, M1R is assumed to be fully "repalmitoylated" as well.

3.3. Single-Protein Tracking as a Function of Palmitoylation State. Representative movies, collected at 25 °C of fluorescently labeled M1P, M1D, and M1R diffusing through solid-supported cushioned POPC lipid membranes are available in the Supporting Information (labeled "M1P movie", "M1D movie", and "M1R movie", respectively). As seen in the movies, there was a very low degree of immobility (2.1%), indicating that the large intracellular domains (N- and C-termini) were most likely orientated away from the solid support. Moreover, it was evident from the movies collected in this study that a dramatic change in the overall mobility of M1P occurred after it was transformed into M1D by HAM. Specifically, the average mobility of M1P was much faster than that observed in the depalmitoylated M1D samples. Moreover, the fast mobility observed for M1P was recovered after product (**3**) in Scheme 1 was "repalmitoylated" forming M1R (product (**6**) in Scheme 1). In addition to the overall mobility of labeled AQP4-M1 in membranes, instances of dimer and trimer formation were clearly observed. Two exemplary frame-by-

https://doi.org/10.1021/acs.jpcb.3c04529
J. Phys. Chem. B 2024, 128, 603−621

frame single-protein tracks leading to dimer and trimer formation are given in Figures 1 and 2, respectively (see Section 4.1 for a detailed discussion about these observations). Other examples can be seen in the raw movies provided in the Supporting Information.

To study this phenomenon in greater detail, each fluorescently labeled protein was individually tracked as described in Section 2.11, and example trajectories are plotted in Figures 3−5A. In these experiments, all samples were

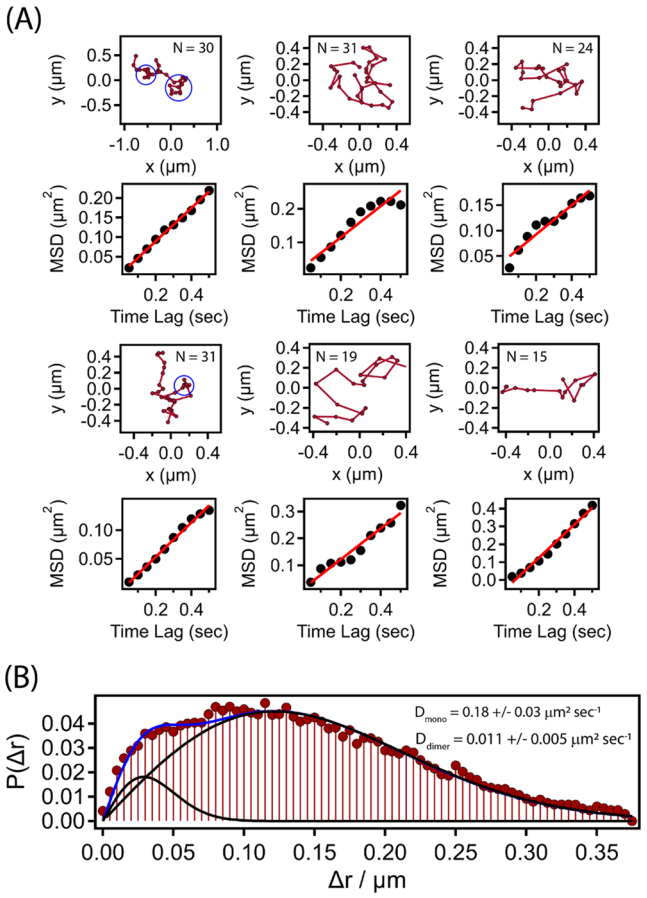

Figure 3. Single-protein tracks and step-size distribution analysis of M1P. (A) Representative single-protein tracks of M1P (top) and their corresponding mean squared displacement curves (bottom). Red dotted lines are the protein trajectory, and blue circles indicate examples of a slowdown in the diffusion of the protein. N indicates the number of frames in the track. In the mean squared displacement plots, the black dotted line represents the experimental mean squared displacement at a time lag, and the solid red line is a linear fit using the function $\langle r^2\,(n\Delta t)\rangle = 4D\,(n\Delta t)$. (B) Experimentally derived step-size distribution (red bars with circular caps) of all M1P tracks. The blue line is an overall two-particle fit (eq 4), while each black curve represents the "slow" (curve left) and "fast" (curve right) populations. D_{mono} is the diffusion coefficient for the fast population (identified as monomers), and D_{dimer} is the diffusion coefficient for the slow population (identified as dimers).

allowed to equilibrate at 37 °C for 60 min before the samples were mounted on the microscope and equilibrated for another 30 min at 37 °C before any data was collected. The movies were then cropped to a uniform size and background-corrected. The squared displacements for each single-protein track at all possible time lags were determined using eq 1

$$(\Delta r_\tau)^2 = (\Delta x_\tau)^2 + (\Delta y_\tau)^2 \tag{1}$$

$$\langle \Delta r_\tau^{\,2}\rangle = \frac{1}{N}\sum_{i=1}^{N} \Delta r_{i,\tau}^{\,2} \tag{2}$$

where $\tau = n\Delta t$ is called the time lag; n is the number of frames for a time lag (τ); and Δt is the time between adjacent frames (50 ms in the current study). [Note: if the frames are adjacent to one another $n = 1$, if its every other frame $n = 2$, if its every third frame $n = 3$, etc.]. Δx_τ and Δy_τ are the spatial displacements in the x and y directions for time lag τ, respectively. The mean-square displacement (MSD) is the average of all steps corresponding to a single time lag τ within the track measured for an individual protein (eq 2), where N is the total number of steps corresponding to time lag τ. Representative MSD vs time lags are plotted under their corresponding trajectories in Figures 3A−5A. The straight line plotted through each MSD vs time lag curve is the theoretical fit for a protein undergoing normal diffusion without interactions that would hinder its free diffusion or cause anomalous diffusion through transient protein−protein interactions. Normal diffusion is given by $\langle \Delta r_\tau^2\rangle = 4D^*\tau$, where D is the diffusion coefficient.

For the M1P and M1R samples, there was a mix of trajectories that display normal diffusion and those that display regions of fast and slow diffusion (anomalous diffusion) within a single trajectory. The latter results in a "wavy" MSD curve rather than a linear curve anticipated for normal diffusion. Moreover, there are many cases in which the trajectories themselves display regions of slow diffusion and regions of faster diffusion (regions of no protein−protein or fleeting protein−protein interactions). The regions of slow diffusion are not always obvious for the palymitoylated samples (M1P and M1R), but some obvious examples are indicated by the blue circles in Figures 3A and 5A. For the depalmitoylated M1D samples most single-protein trajectories show clear regions of fast and slow diffusion and very few tracks with linear MSD curves were observed (Figure 4A). Because of these complex diffusion characteristics, diffusion coefficients were not obtained by simple fits of the MSD curves.

Instead, an alternative method that uses the probability distribution of the spatial displacement of proteins between adjacent frames (step-size distribution analysis) was used to determine diffusion coefficients. This method generates a histogram from the step sizes between adjacent frames for all particles tracked. These histograms were then divided by the overall area under the curve to generate a probability distribution. For a particle undergoing Brownian motion, the probability distribution for a protein moving a distance Δr in each time interval Δt is given by eq 3[46]

$$P(\Delta r) = \left(\frac{\Delta r}{2D\cdot\Delta t}\right) e^{-\Delta r^2/4D\Delta t} \tag{3}$$

where Δr is the step size, D is the diffusion coefficient, and Δt is the time between frames. For multiple types of diffusing particles (monomer, dimers, trimers, etc.), the step-size probability distribution is given by eq 4[32]

$$P(\Delta r) = \sum_i f_i \left(\frac{\Delta r_i}{2D_i\cdot\Delta t}\right) e^{-\Delta r_i^2/4D_i\Delta t} \tag{4}$$

https://doi.org/10.1021/acs.jpcb.3c04529
J. Phys. Chem. B 2024, 128, 603−621

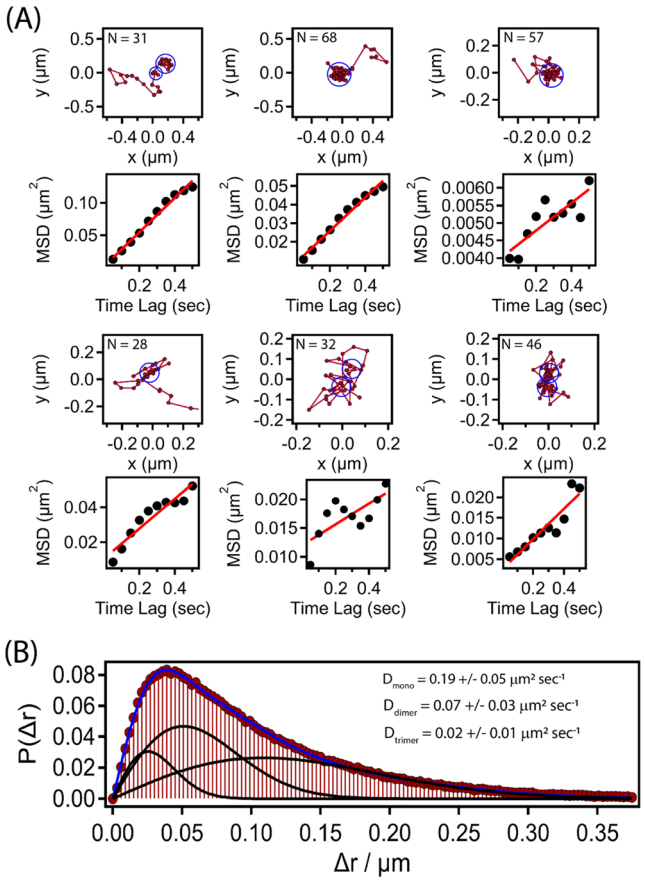

Figure 4. Single-protein tracks and step-size distribution analysis for M1D. (A) Representative single-protein tracks of M1D (top) and their corresponding mean squared displacement curves (bottom). Red dotted lines are the protein trajectory, and blue circles indicate examples of a slowdown in the diffusion of the protein. *N* indicates the number of frames in the track. In the mean squared displacement plots, the black dotted line represents the experimental mean squared displacement at a time lag and the solid red line is a linear fit using the function $\langle r^2\ (n\Delta t)\rangle = 4D\ (n\Delta t)$. (B) Experimentally derived step-size distribution (red bars with circular caps) of all M1D tracks. The blue line is an overall three-particle model fit (eq 4), while each black curve represents the "slow" (curve left), "intermediate" (curve center), and "fast" (curve right) populations. D_{mono} is the diffusion coefficient for the fast population (identified as monomers), D_{dimer} is the diffusion coefficient for the intermediate population (identified as dimers), and D_{trimer} is the diffusion coefficient for the slow population (identified as trimers).

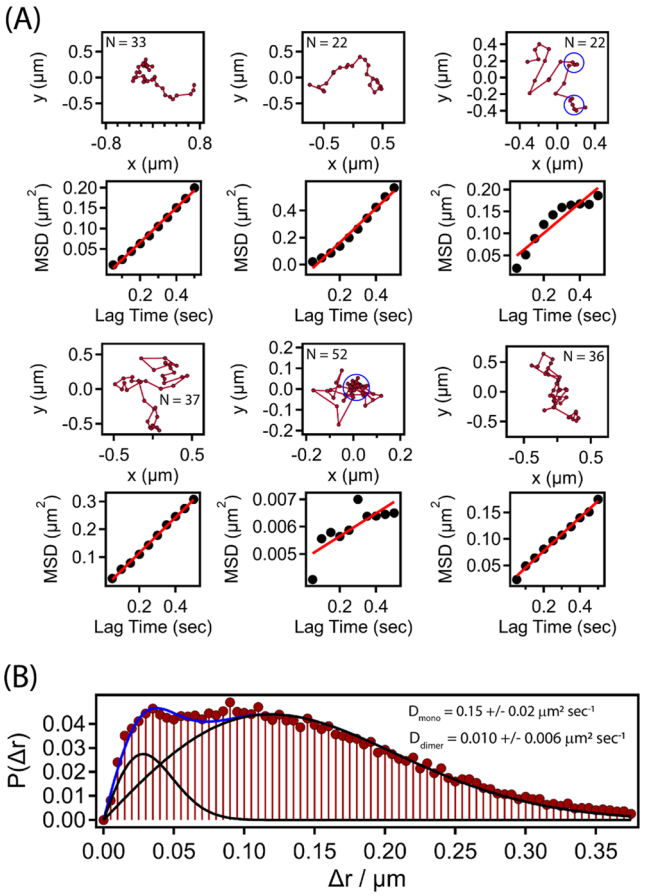

Figure 5. Single-protein tracks and step-size distribution analysis of M1R. (A) Representative single-protein tracks of M1R (top) and their corresponding mean squared displacement curves (bottom). Red dotted lines are the protein trajectory, and blue circles indicate examples of a slowdown in the diffusion of the protein. *N* indicates the number of frames in the track. In the mean squared displacement plots, the black dotted line represents the experimental mean squared displacement at a time lag and the solid red line is a linear fit using the function $\langle r^2\ (n\Delta t)\rangle = 4D\ (n\Delta t)$. (B) Experimentally derived step-size distribution (red bars with circular caps) of all M1P tracks. The blue line is an overall two-particle fit (eq 4), while each black curve represents the "slow" (curve left) and "fast" (curve right) populations. D_{mono} is the diffusion coefficient for the fast population (identified as monomers), and D_{dimer} is the diffusion coefficient for the slow population (identified as dimers).

where f_i is the fractional population of each type of diffusing particle assuming each undergoes Brownian motion.

The step-size distributions and results of the analysis for M1P, M1D, and M1R are given in Figures 3B−5B, respectively. All measured distributions displayed more than one Brownian diffuser and were fitted using eq 4, where *i* is set to a minimum number of distinct diffusing particles as possible (Figures 3−8). The palymitoylated samples, M1P and M1R, were successfully fit to a model of two distinct diffusing particles ($i = 2$), while the step-size distribution for M1D had to be fit to a minimum three-particle model ($i = 3$).

The diffusion coefficients obtained at 37 °C from the step-size distribution analysis for M1P were $D^{M1P}_{mono} = 0.18 \pm 0.03\ \mu m^2\ s^{-1}$ for the fast component and $D^{M1P}_{dimer} = 0.011 \pm 0.005\ \mu m^2\ s^{-1}$ for the slow component. As discussed below, the fast component is taken to be a single aquaporin tetrameric unit (monomer) and the slow component is taken to be a dimer of two tetrameric units (dimer). After repalmitoylation, the diffusion coefficients for M1R were $D^{M1P}_{mono} = 0.15 \pm 0.02\ \mu m^2\ s^{-1}$ for the fast component and $D^{M1P}_{dimer} = 0.010 \pm 0.006\ \mu m^2\ s^{-1}$ for the slow component. These are statistically the same as that observed for M1P. These results, along with the two-component step-size distribution, reinforce the conclusion that repalmitoylated M1R behaves in a similar manner to the unmodified M1P isotype. The reported diffusion coefficients and standard deviations were calculated from an average of 4 independent experiments each conducted at 37 °C.

As reported above, the depalymitoylated M1D distribution could not be fit using only two populations. Choosing the smallest value of $i = 3$ in eq 4 that successfully fits this distribution (Figure 4B), gives three diffusion coefficients: $D^{M1P}_{mono} = 0.19 \pm 0.04\ \mu m^2\ s^{-1}$, $D^{M1P}_{dimer} = 0.07 \pm 0.03\ \mu m^2\ s^{-1}$, $D^{M1P}_{trimer} = 0.02 \pm 0.01\ \mu m^2\ s^{-1}$ (see trimer discussion in Section

https://doi.org/10.1021/acs.jpcb.3c04529
J. Phys. Chem. B 2024, 128, 603−621

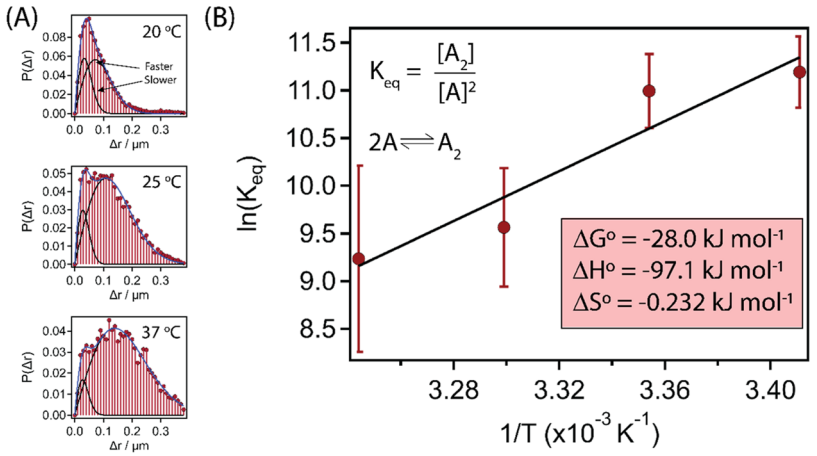

Figure 6. van't Hoff analysis of M1P. (A) Step-size probability distributions of M1P (red bars with circle caps) at the experimental temperature indicated in the top right corner of the plot. Blue curves are the overall two-particle fit, with the black curves representing the "slow" and "fast" populations. Black arrows indicate the different population curves. (B) van't Hoff plot of $\ln(K_{eq})$ vs $1/T$. The temperature points in the plot are at 20, 25, 30, and 37 °C. The equilibrium expression and the reaction scheme are indicated at the top left of the plot. Red dots are the experimental data, and the error bars are calculated from triplicate experiments. The black line is the fit using eq 12. $\Delta H°$ and $\Delta S°$ were determined from the slope and intercept of the linear fit, and $\Delta G°$ was determined from $\Delta G° = \Delta H° - T\Delta S°$. The error for $\Delta G°$, $\Delta H°$, and ΔS is given in Table 1.

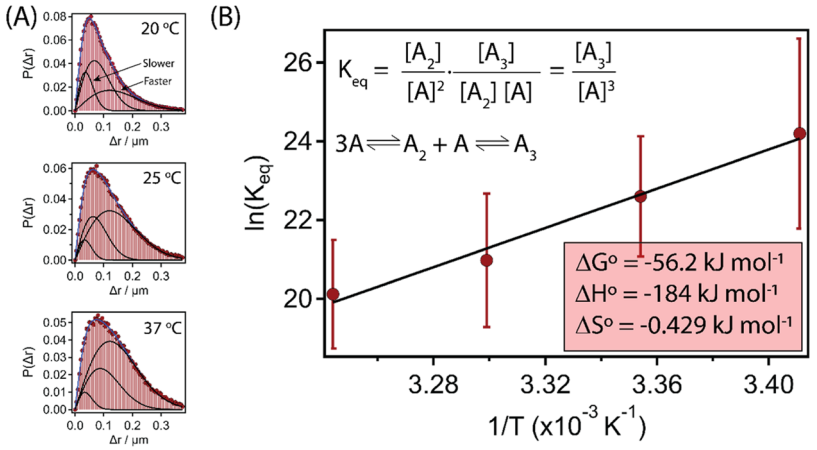

Figure 7. van't Hoff analysis of M1D. (A) Step-size probability distributions of the M1D (red bars with circle caps) at the experimental temperature indicated in the top right corner of the plot. Blue curves are the overall three-particle fit, with the black curves representing the "slow" "intermediate" and "fast" populations. Black arrows indicate the different populations. (B) van't Hoff plot of $\ln(K_{eq})$ vs $1/T$. The temperature points in the plot are at 20, 25, 30, and 37 °C. The equilibrium expression and reaction scheme are indicated at the top left of the plot. Red dots are the experimental data, and the error bars are calculated from triplicate experiments. The black line is the fit using eq 12. $\Delta H°$ and $\Delta S°$ were determined from the slope and intercept of the linear fit, and $\Delta G°$ was determined from $\Delta G° = \Delta H° - T\Delta S°$. The error for $\Delta G°$, $\Delta H°$, and ΔS is given in Table 2.

4.1). Even though a comparison of palmitoylated and depalmitoylated samples can be made, these comparisons are imperfect because the N-terminal tails for M1D are not pinned to the lipid membrane by palmitoylation groups as in M1P and M1D (see Figures 9 and 10). Because the N-terminal tails do not have palmitoylation groups, it is expected that M1D would have less drag in the membrane (as compared to M1P). Moreover, a monomer has a total of 4 N-terminal tails, dimers have 8 N-terminal tails and trimers have a total of 12 N-terminal tails, so the difference in diffusion coefficients between palmitoylated and depalmitoylated samples would be more pronounced for oligomers. Nevertheless, the measured diffusion coefficients for the fast-moving particles in the M1D samples were statistically the same as the fast-moving particles in the palmitoylated samples. However, the intermediate particles in the M1D samples were statistically faster than the slow-moving particles in the palymitoylated sample. Finally, the diffusion coefficient of the slowest-moving particles in M1D is larger but statistically similar to the slow-moving M1P particles.

3.4. Temperature Dependence Observed in Step-Size Distributions. The fractional populations of slower and faster diffusing particles were temperature-dependent for all AQP4-M1s. The "slower" moving particles are characterized by the distribution with the smallest average step sizes, and the "faster" moving particles are characterized by the distribution with the larger average step sizes (see Figures 6A–8A). Figure 6A plots the step-size distributions for M1P at 20, 25, and 37 °C. As described above, the step-size distribution could be fit to a minimum of two types of diffusing particles using eq 4 with $i = 2$. As the temperature increased, the fractional population of slower-moving particles decreased, and the fractional population of faster-moving particles increased. This held true for M1R as well (Figure 8A). For the depalmitoylated

https://doi.org/10.1021/acs.jpcb.3c04529
J. Phys. Chem. B 2024, 128, 603–621

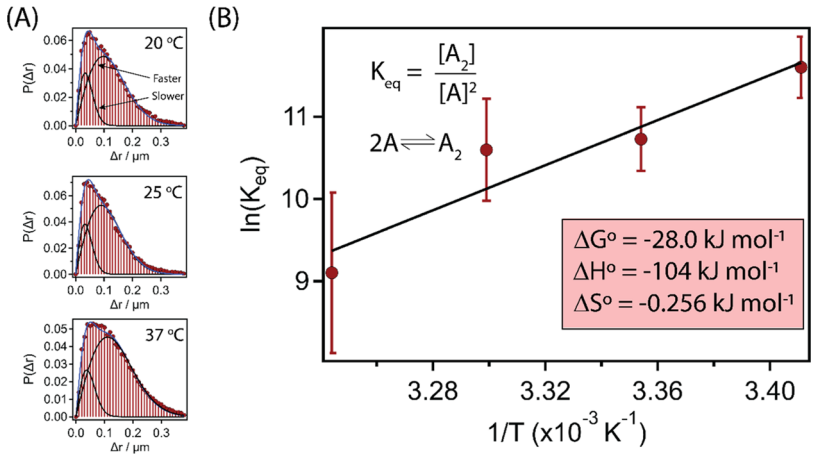

Figure 8. van't Hoff analysis of M1R. (A) Step-size probability distributions of M1R (red bars with circle caps) at the experimental temperature indicated in the top right corner of the plot. Blue curves are the overall two-particle fit, with the black curves representing the "slow" and "fast" populations. Black arrows indicate the different population curves. (B) van't Hoff plot of $\ln(K_{eq})$ vs $1/T$. The temperature points in the plot are at 20, 25, 30, and 37 °C. The equilibrium expression and the reaction scheme are indicated at the top left of the plot. Red dots are the experimental data, and the error bars are calculated from triplicate experiments. The black line is the fit using eq 12. $\Delta H°$ and $\Delta S°$ were determined from the slope and intercept of the linear fit, and $\Delta G°$ was determined from $\Delta G° = \Delta H° - T\Delta S°$. The error for $\Delta G°$, $\Delta H°$, and ΔS is given in Table 1.

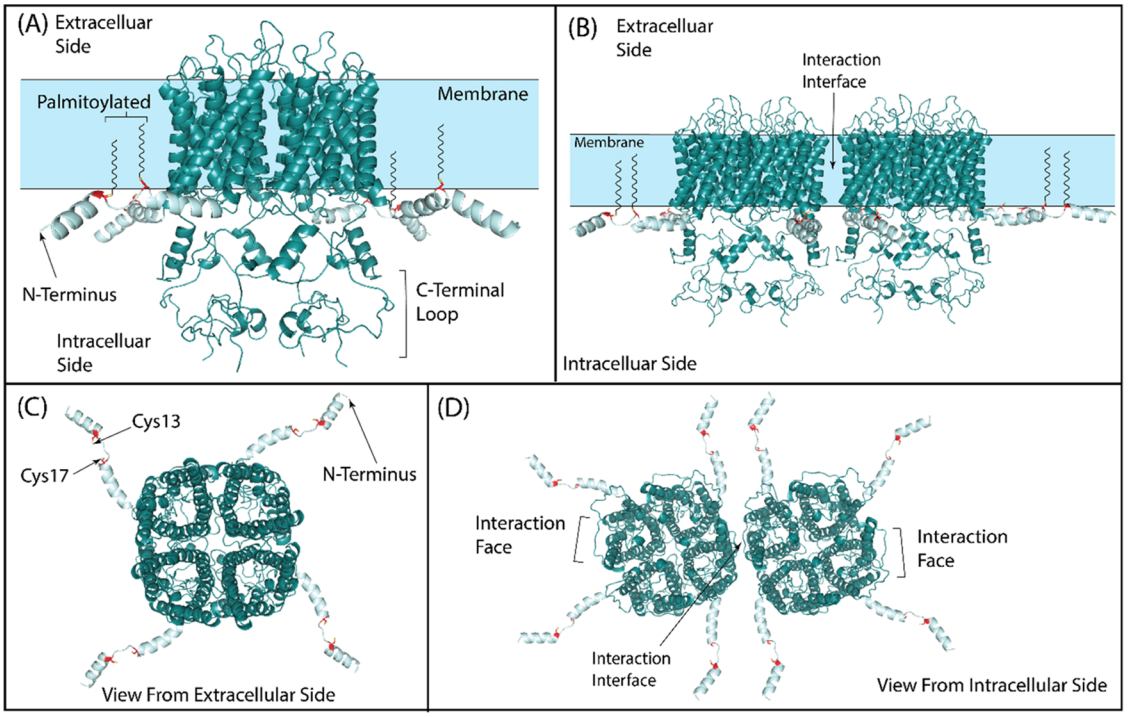

Figure 9. Predicted and modified structure of M1P and an M1P dimer. (A) A single M1P integrated into the membrane (blue bar). The red amino acids indicate the location of solvent-accessible cysteine residues. The carbon chains on the cysteine residues represent the palmitoyl lipid groups integrated into the membrane. The black arrow points to the N-terminus, and the C-terminus is labeled on the intracellular side. (B) An M1P dimer integrated into the membrane. The black arrow points to the interaction interface, where the individual tetramers bind to form the dimer. (C) Top view (from the extracellular side) of a single M1P showing the configuration of the N-terminus which minimizes the steric hindrance while still being pinned to the membrane by the palmitoyl lipids attached to cysteine-13 and -17, indicated by the black arrows. (D) Bottom view (from the intracellular side) of an M1P dimer. The interaction faces are highlighted, and the black arrow indicates the interaction interface that forms the dimer.

samples (M1D), the step-size distribution (Figure 7A) was once again fit to eq 4 with $i = 3$ at all temperatures. For M1D, the fractional population of the slower and intermediate moving particles decreased, and the fractional population of faster-moving particles increased with increasing temperature (Figure 8).

3.5. Structure Predictions of Palmitoylated and Depalmitoylated AQP4. Rat AQP4 and human APQ4 share 94% sequence identity and 96% sequence similarity, and they would, presumably, have very similar structures. The 2D structure of rat AQP4 solved using electron crystallography forms an array of repeating AQP4s.[44] The arrays were then used to model the hypothetical structures of dimers and

https://doi.org/10.1021/acs.jpcb.3c04529
J. Phys. Chem. B 2024, 128, 603−621

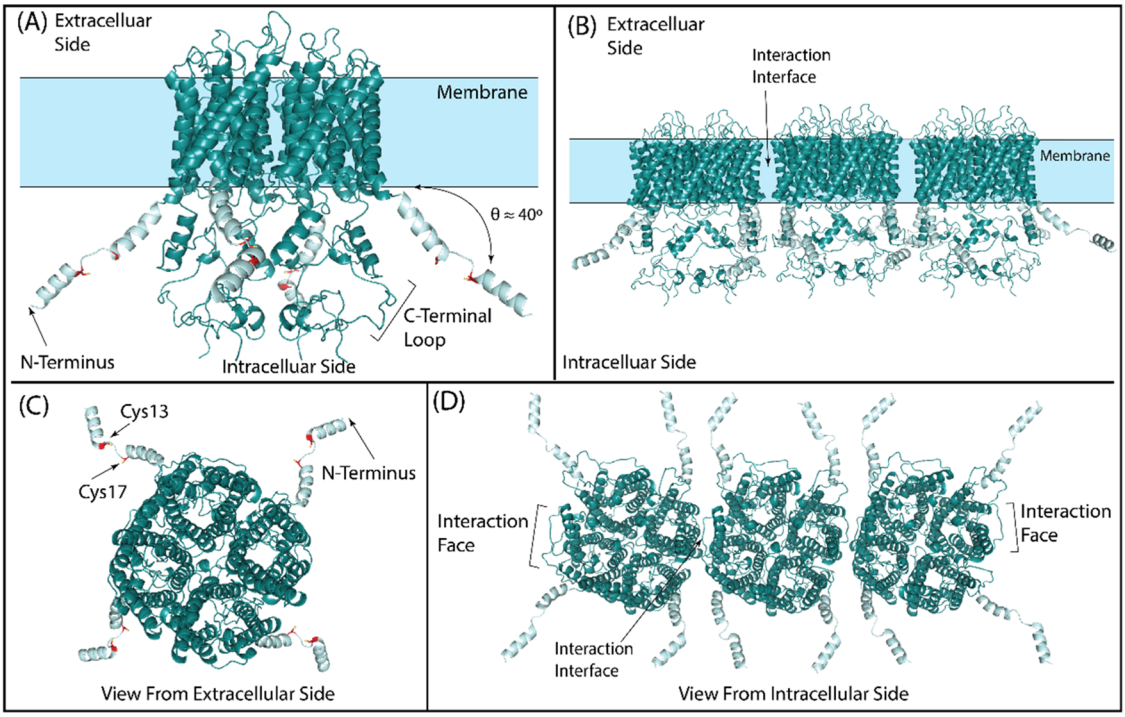

Figure 10. Predicted and modified structure of M1D and an M1D trimer. (A) A single M1D integrated into the membrane (blue bar). The red amino acids indicate the location of solvent-accessible cysteine residues. The black arrow is pointing to the N-terminus, and the C-terminus is labeled on the intracellular side. (B) An M1D trimer integrated into the membrane. The black arrow points to one of the interaction interfaces, where the individual tetramers bind to form the trimer. (C) Top view (from the extracellular side) of a single M1D. The black arrows point to the N-terminus, and the red highlighted cysteine-13 and -17 residues. The decrease in steric hindrance in the system causes the N-terminus to be more compact than M1P. (d) Bottom view (from the intracellular side) of an M1D trimer. The possible binding faces are highlighted, and the black arrow indicates one of the interaction interfaces that form the trimer.

trimers with each AQP4 slightly staggered relative to the adjacent AQP4 (Figures 9 and 10). Given the electron crystal data, a hydrogen-bond network is formed between a tyrosine and an arginine of adjacent AQP4s in addition to predicted van der Waals interactions between two isoleucines and a glycine/tryptophan pair (Figure 11).[44] It is also noted that at the interface between adjacent AQP4s, the sequence between human and rat is completely conserved.

It is unknown if palmitoylation causes a conformational change; however, we hypothesize that significant movement does occur in the N-terminal region to allow for the insertion of the palmitoylation groups into the membrane. Presumably, the cysteines would reside in the intracellular space before palmitoylation by palmitoyl acyltransferase. The N-terminal region would then swing toward the membrane as the palmitoylation groups are attached. Figure 9 represents a hypothetical conformation of the N-terminal tail that is restricted to the plane of the membrane by the *S*-palmitoylation group inserted into the intercellular leaflet of the lipid bilayer. The placing of the palymitoylated N-terminal tail on the membrane was done in such a way to minimize the steric interactions.

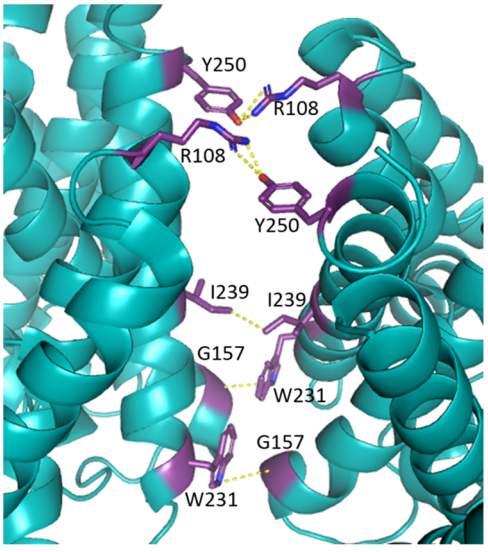

Figure 11. Rat AQP4 solved structure indicating protein−protein interactions between two AQP4 at the interaction interfaces. Amino acid residues involved in the binding interactions are highlighted in purple and labeled with their respective amino acid single-letter code and position. The yellow dotted lines indicate the two amino acids that are interacting.

4. DISCUSSION

4.1. Identification of AQP4-M1 State to the Populations of Diffusing Particles. There are several observations that help identify the nature of the different diffusing particles in these studies. The primary means of identification comes from direct observation. The movies supplied in the Supporting Information clearly show many examples of particles diffusing in the membrane, which then co-localize and diffuse as a single unit, and then dissociate (in many cases). An exemplary track taken from the M1P sample set at 15 °C is plotted in Figure 1. In this example, a total of 16 frames are plotted. In the first 6 frames, two particles are

https://doi.org/10.1021/acs.jpcb.3c04529
J. Phys. Chem. B 2024, 128, 603−621

highlighted by red and blue circles, with the integrated intensity of each particle recorded within the parentheses (in grayscale $\times 10^{-6}$). Starting at frame 7, the two particles bind to one another as indicated by their co-localization (green circle) and diffusion as a single unit. The fluorescence signal of the bound dyad is approximately twice as bright as the individual particles in frames 1−6 as expected from dimer formation. The dyad state continues until frame 13 at which point the particles clearly dissociate and diffuse separately in the membrane. The fluorescent intensity of the individual particles in frames 13−16 decreases to the intensity seen in frames 1−6, indicating the reversibility of the process. Note that each AQP4-M1 monomer has, on average, four fluorophores attached to it, dimers will have 8, and trimers will have 12. Therefore, dimers will fluoresce more than monomers and trimers will fluoresce more than dimers. Moreover, upon dimer (or trimer) formation the change in the value of the diffusion coefficient will be negative (i.e., the resultant diffusion coefficient of the newly formed dimer will be smaller than the average of the constituent monomers).

Plotted below the single-molecule fluorescence images in Figure 1 are three MSD vs time lag curves. In this analysis, the MSDs were calculated separately (eq 2) for frames 1−6, 7−12, and 13−18 and plotted against the time lag for each of the three segments of the tracks as indicated in the plots. These plots clearly demonstrate that the individual particles (frames 1−6) move with a larger diffusion coefficient than the dimer (frames 7−12), and after dissociation, the individual particles regain their mobility (frames 13−18). These observations have led to the conclusion that the least bright, faster-moving particles are AQP4-M1 monomers and the bright, slower-moving particles are dimers. This conclusion is reinforced by the bimodal nature observed in the step-size distribution for M1P and M1R (Figures 3 and 5) and the temperature-dependent studies which show that as the fractional population of fast-moving particles increases, there is a concomitant decrease in slow-moving particles. This indicates that the monomers and dimers are at equilibrium with one another.

Direct observation in the M1D sample set shows a greater degree of association between particles than that observed in the palmitoylated sample sets. This higher degree of association leads to higher-order oligomer formation. Figure 2 is an example of trimer formation in which two particles are tracked in frames 1−5; one of the particles is indicated by a red circle and the other blue. In frame 6, these two particles co-localize and move as a single unit. In doing so, the intensity of the dyad is approximately twice that of the individual particles. Also depicted in frame 6 is a third particle (purple) with a measured fluorescence intensity approximately the same as those tracked in frames 1−5. In frame 11, the third particle (purple) co-localizes with the dyad formed in frame 6 (green) to form a triad that moves as a single unit until frame 15 with an average fluorescence intensity approximately three times that of the least bright particles. Below the images are the MSD vs time lag for each particle in frames 1−5, 6−10, and 11−15 (the curves are color-coded corresponding to the particles in the images). This data clearly shows that the least bright particles have the highest diffusion coefficients, the dyad in frames 6−10 has the second highest diffusion coefficient, and the triad has the smallest diffusion coefficient. This leads to the conclusion that the fast and least bright particles are monomers, the intermediate moving particles with a fluorescence intensity twice that of the monomers are dimers, and the slowest-moving particles with the brightest fluorescence intensity are trimers. This conclusion is reinforced by the step-size distributions plotted in Figures 4B and 7A and the fact that the three measured diffusion coefficients are all statistically different from one another. This adds weight to the conclusion that at least three different particles exist in the overall population. Finally, the temperature dependence shows that as the fast monomer population increases with temperature, the dimer and trimer populations decrease. This temperature dependence and direct observations show that they are all in equilibrium with one another.

4.2. Equilibrium Constants for Dimer and Trimer Formation. Referring to Section 4.1, the equilibrium equation between monomers and dimers in the M1P and M1R sample sets is given by

$$2[\mathrm{AQPM1}]_4 \rightleftharpoons [[\mathrm{AQPM1}]_4]_2 \tag{5}$$

and the equilibrium constant is given by

$$K_{\mathrm{eq}} = \frac{(\theta_{\mathrm{dimer}}/\theta^\circ)}{(\theta_{\mathrm{mono}}/\theta^\circ)^2} \tag{6}$$

where θ_{mono} and θ_{dimer} are two-dimensional number densities of the monomers and dimers in units of number of particles cm^{-2}, respectively, and θ° is the standard state number density. The standard state number density is taken to be 2.1×10^{12} particles cm^{-2}, which is the maximum number of AQP4-M1s needed to completely fill the sample surface; calculated from the lattice spacing reported by Rash et al.[26] The observation that the AQP4 molecules are defusing on the surface indicates that they should be treated as a gas rather than a lattice.[47] Given the very small values of theta used in this study ($\theta_{\mathrm{mono}}/\theta^0 \sim 5.0 \times 10^{-6}$), an ideal gas treatment seems the most appropriate simple model.

The number densities in eq 6 are calculated from the measured fractional populations obtained from fitting the step-size distribution to eq 4 and the total number density of measured monomers plus dimers from the relationships below

$$\theta_{\mathrm{mono}} = f_{\mathrm{mono}} \times \frac{\text{total number of particles}}{\mathrm{cm}^2} \tag{7}$$

$$\theta_{\mathrm{dimer}} = f_{\mathrm{dimer}} \times \frac{\text{total number of particles}}{\mathrm{cm}^2} \tag{8}$$

where f_{mono} and f_{dimer} are the fractional populations of the monomers and dimers, respectively. If we take the standard state temperature to be 298.15 K, the measured equilibrium constants for dimer formation in M1P and M1R are $K^\circ_{\mathrm{eq,\ M1P}} = 4.01 \times 10^4$ and $K^\circ_{\mathrm{eq,\ M1R}} = 4.90 \times 10^4$, respectively. The free energies were then calculated from $\Delta G^\circ = -RT\ln(K^\circ_{\mathrm{eq}})$ to give $\Delta G^\circ_{\mathrm{eq,\ M1P}} = -26.3$ kJ mol^{-1} and $\Delta G^\circ_{\mathrm{eq,\ M1R}} = -26.8$ kJ mol^{-1}. These are close to the free energies obtained from a van't Hoff analysis (Section 4.2) and nearly identical to each other. The measured free energy for M1R gives further evidence that chemical repalmitoylation can restore the dimer-forming properties of AQP4-M1 after the chemical depalmitoylation step in Scheme 1.

For M1D (depalmitoylated), the trimodal nature of the step-size distribution analysis led to the conclusion that there is an equilibrium between monomers, dimers, and trimers at the very least. But it should be noted that it is possible that higher-ordered oligomers are present in the samples. This study produced no strong evidence of any significant population of

https://doi.org/10.1021/acs.jpcb.3c04529
J. Phys. Chem. B 2024, 128, 603−621

Table 1. Standard State Thermodynamic Quantities of Dimer Formation

	2(AQPM1) ⇌ $(AQPM1)_2$			
dimer formation	$\ln(K^\circ_{eq})$	ΔG° (kJ mol^{-1})	ΔH° (kJ mol^{-1})	ΔS° (kJ mol^{-1})
M1P*	10.6 ± 0.6	−26.3 ± 1.6	−97.1 ± 12	−0.232 ± 0.030
M1R*	10.8 ± 0.4	−26.8 ± 1.0	−104 ± 17	−0.256 ± 0.058
AQP4-M1** (elliptical cylinder)	9.54	−23.6	−101	−0.258
AQP4-M1** (cuboid)	9.40	−23.3	−101	−0.259
AQP4-M1*** (no rotational degree of freedom)	19.0	−47.0	−101	−0.179

*Standard deviations of ΔH° and ΔS° for M1P and M1R were calculated from the fit of the van't Hoff analysis. The standard deviation for ΔG° was calculated from $\Delta G^\circ = -RT\ln(K^\circ_{eq})$ at 298.15 K from three independent experiments. Standard state is taken to be T = 298.15 K and $\theta^\circ = 2.1 \times 10^{12}$. **$\Delta G^\circ$, ΔH°, and ΔS° were calculated from eqs 18, 19, and 20 with the parameters from Table 3. ***ΔG°, ΔH°, and ΔS° were calculated from eqs 26, 27, and 28 with the parameters from Table 3

Table 2. Standard State Thermodynamic Quantities of Trimer Formation

	3(AQPM1) ⇌ $(AQPM1)_2$ + (AQPM1) ⇌ $(AQPM1)_3$			
trimer formation	$\ln(K^\circ_{eq})$*	ΔG° (kJ mol^{-1})*	ΔH° (kJ mol^{-1})*	ΔS° (kJ mol^{-1})*
M1D*	22.7 ± 1.5	−56.2 ± 3.7	−184 ± 21	−0.429 ± 0.088
AQP4-M1** (elliptical cylinder)	18.4	−45.7	−201**	−0.521
AQP4-M1** (cuboid)	18.1	−45.0	−201**	−0.524
AQP4-M1*** (no rotational degree of freedom)	37.7	−93.4	−201***	−0.361

*Standard deviations of ΔH° and ΔS° for M1D were calculated from the fit of the van't Hoff analysis. The standard deviation for ΔG° was calculated from $\Delta G^\circ = -RT\ln(K^\circ_{eq})$ at 298.15 K from three independent experiments. The standard state is taken to be T = 298.15 K and $\theta^\circ = 2.1 \times 10^{12}$ **ΔG°, ΔH°, and ΔS° were calculated from eqs 23, 24, and 25 with the parameters from Table 3. ***ΔG°, ΔH°, and ΔS° were calculated from eqs 29, 30, and 31 with the parameters from Table 3.

oligomers greater than the observed trimer population and was thus precluded from the thermodynamic analysis. The chemical equation for the process is given by

$$3[AQPM1]_4 \rightleftharpoons [[AQPM1]_4]_2 + [AQPM1]_4 \rightleftharpoons [[AQPM1]_4]_3 \quad (9)$$

and the equilibrium constant is given by

$$K_{eq} = \frac{(\theta_{dimer}/\theta^\circ)}{(\theta_{mono}/\theta^\circ)^2} \times \frac{(\theta_{trimer}/\theta^\circ)}{(\theta_{mono}/\theta^\circ) \times (\theta_{dimer}/\theta^\circ)} = \frac{(\theta_{trimer}/\theta^\circ)}{(\theta_{mono}/\theta^\circ)^3} \quad (10)$$

where θ_{trimer} is the two-dimensional number density for the trimers. As described above, the trimer number density is determined by the fractional population of the slowest-moving particles in the step-size distribution for the M1D sample sets and the total number of particles counted in an experiment.

$$\theta_{trimer} = f_{trimer} \times \frac{\text{total number of particles}}{\text{cm}^2} \quad (11)$$

For the depalmitoylated samples at 298.15 K, the experimentally determined equilibrium constant and Gibbs free energy is $K^\circ_{eq,\ M1D} = 6.87 \times 10^9$ and $\Delta G^\circ_{eq,\ M1D} = -56.1$ kJ mol^{-1}. The measured free energy for the formation of the trimer is ∼2.1 times that seen in dimer formation. These results lead to the hypothesis that the trimers are formed from two nearly identical protein−protein interactions, but palmitoylation at Cys-13 and Cys-17 prevents the formation of trimers by sterically blocking additional monomers from coming together (see discussion below).

4.3. Gibbs Free Energy, Enthalpy, and Entropy of Formation. As described in Section 3.4, the equilibrium populations of monomers, dimers, and trimers are temperature-dependent as expected. The temperature dependence is reflected in the van' Hoff relationship (eq 12), which was used to determine all thermodynamics driving forces (ΔG°, ΔH°, and ΔS°);

$$\ln(K_{eq}) = -\frac{\Delta H^\circ}{RT} + \frac{\Delta S^\circ}{R} \quad (12)$$

where ΔH° is the standard state enthalpy, ΔS° is the standard state entropy, and R is the ideal gas constant. $\Delta G^\circ = \Delta H^\circ - T\Delta S^\circ$ was used to determine standard state free energies from ΔH° and ΔS° and give nearly identical results to the free energies calculated from $\Delta G^\circ = -RT\ln(K^\circ_{eq})$. The results of the analysis are shown in Figures 6−8B and recorded in Tables 1 and 2. In all cases, the van't Hoff plots were linear and ΔG°, ΔH°, and ΔS° for trimer formation were about twice that measured for dimer formation.

To explain this phenomenon, first recall that all AQP 4s have a square topology with rounded corners. Moreover, published X-ray crystallography and cryo-electron microscopy studies show that, for the M23 isoforms, AQP4s will crystallize and form OAPs through the interfacial interaction shown in Figures 9D and 10D.[25,27] [Note: There are 4 interaction faces per AQP4 homotetramer, and in the case of the M23 isoform, each face will interact with an adjacent M23 to form an OAP.] For all AQP4-M1s studied, it is reasonable to hypothesize that the same interaction would also be responsible for dimer and trimer formation. However, the growth of these oligomers would be limited by the steric interactions of the longer N-terminal tail, which will be amplified when palmitoylated. If the dimer is held together by a single interface and a trimer is held together by two interfaces, Hess's law also would dictate that ΔG°, ΔH°, and ΔS° would approximately double, in agreement with experimental data. Moreover, smaller enthalpy values would also be expected as steric hindrance increases, limiting its growth to small oligomers.

Figures 9 and 10 depict hypothetical structures that include both the N- and C-terminal regions of the protein as well as

https://doi.org/10.1021/acs.jpcb.3c04529
J. Phys. Chem. B 2024, 128, 603−621

likely interfaces for dimer and trimer formation. The hypothetical structures were created using the structure prediction software described in Sections 2.12 and 3.5. For palmitoylated AQP4-M1, the N-terminal tails were restricted to move in the plane of the membrane and arranged to minimize steric interactions. For depalmitoylated AQP4-M1, the N-terminal tails were not constrained to the membrane surface but were allowed to move out of the plane to minimize steric interactions. The protein−protein interfaces were assumed to be the same as the known packing seen in X-ray or electron crystal structures and in cryo-electron microscopy images of AQP4-M23.

Consider the predicted structure for M1P in Figure 9. According to this structure, the N-termini closest to the interaction interface will have to take up a configuration slightly tilted away from the interface to minimize steric interactions. This, in turn, will block the interfaces perpendicular to a newly formed dimer. This suggests that a trimer will predominantly form at an interface directly opposite that of dimer formation. Experimental evidence presented above leads to the conclusion that M1P and M1R can form dimers only, but some of the steric interference is relieved after depalmitoylation; this leads to trimer formation, as depicted in Figure 10 for M1D in which the N-terminal tail can rotate ∼40° out of the plane of the membrane. Because dimer formation blocks the perpendicular interface, trimers are most likely to form in a straight line to have the least steric interactions. The symmetry of a trimer formed in this manner would lead to a doubling of the thermodynamics driving forces as observed from experiment.

Figure 11 depicts the protein−protein interactions of APQ4-M23 along the interaction interfaces illustrated in Figures 9 and 10.[44] Along this interface are two hydrogen bonds formed between the R108s and Y250s on each adjacent AQP4 monomer. Moreover, three possible van der Waals interactions exist between close-contact amino acids: one between the I239−I239 and two between the G157−W231 residues on adjacent AQP4 monomers. A crude estimate for the change in enthalpy upon AQP4-M1 dimer formation can be made by simply adding up all possible enthalpic contributions between residues at the interaction interface. This can be accomplished using literature values for specific amino pairs. For the R108−Y250 grouping, we used the measured enthalpy change between phenol/guanidine complexes (in a nonaqueous environment) measured by Banyikwa et al., which is $\Delta H \sim$ 74 kJ/mol per hydrogen bond.[48] The van der Waals interaction between I239 and I239 was estimated to be $\Delta H \sim$ 3.3 kJ/mol based on the enthalpies measured for leucine zippers[49] and $\Delta H \sim$ 0.1 kJ/mol for the interactions between G157 and W231.[50] Taken together, the total crude estimate for the change in enthalpy for dimer formation is $\Delta H_{\text{estimate}} \sim -151$ kJ/mol. It is noted that this estimate describes optimal residue interactions between groupings, and the enthalpy of hydrogen-bond formation in aqueous environments is significantly lower than in nonaqueous environments;[51] nevertheless, the crude estimation gives an upper limit to ΔH. Given these limitations, the measured ΔH for AQPM1 dimer formation ($\Delta H \sim$ 101 kJ/mol) is in rough agreement with the structural models suggested in Figures 9 and 10.

4.4. Statistical Mechanical Model for AQP4-M1 Interactions. By treating AQP4-M1 as a two-dimensional gas, one can estimate the thermodynamic driving forces for dimer and trimer formation for comparison with experimental values. The statistical mechanical model described below accounts for translations, rotations, and the interaction potential between adjacent AQP4-M1s in dimers and trimers. The vibrational degrees of freedom contribute little to $\Delta G°$, $\Delta H°$, and $\Delta S°$ and are ignored in this model (see the Supporting Information for the justification of this approximation). Given that the ensemble is treated as a two-dimensional ideal gas, the following general expressions hold true

$$Q_j = \frac{q_j^{N_j}}{N_j!} \tag{13}$$

where Q_j is the partition function; j denotes monomer, dimer, or trimer; N_j is the number of monomers, dimers, or trimers in the ensemble; and q_j is the overall molecular partition function. The overall molecular partition function is simply the product of the molecular partition functions for each degree of freedom $q_j = q_{j,\text{trans}}{}^{*}q_{j,\text{rot}}{}^{*}q_{j,\text{interaction}}$. The molecular partition function for translations ($q_{j,\text{trans}}$) is given by

$$q_{j,\text{trans}} = \frac{2\pi m_j T a}{h^2} = \lambda_j T a \tag{14}$$

and,

$$\lambda_j = \frac{2\pi m_j}{h^2} \tag{15}$$

where m_j is the mass in kg of the monomer, dimer, or trimer; T is the temperature; a is the area of the ensemble; k is the Boltzmann constant; and h is Planck's constant. As stated earlier, this is appropriate for the very low values of (a/N) observed.[47] If $\lambda_{\text{monomer}} = \lambda$, then $\lambda_{\text{dimer}} = 2\lambda$ and $\lambda_{\text{trimer}} = 3\lambda$. There are two translational degrees of freedom (x and y). The molecular partition function for rotations ($q_{j,\text{rot}}$) is given by

$$q_{j,\text{rot}} = \left(\frac{T}{\theta_{j,\text{rot}}}\right)^{1/2} \tag{16}$$

where $\theta_{j,\text{rot}}$ is the rotational temperature given by

$$\theta_{j,\text{rot}} = \frac{\hbar^2}{2I_j k} \tag{17}$$

where I_j is the moment of inertia along the direction perpendicular to the membrane surface for monomers, dimers, or trimers. There is only one rotational degree of freedom with its principal axis perpendicular to the membrane. The molecular partitional function for the interaction between adjacent AQP4-M1s ($q_{j,\text{interaction}}$) is given by

$$q_{j,\text{interaction}} = e^{-\Delta_j/kT}$$

where $\Delta_j = 0$ for monomers, $\Delta_j = \Delta$ for dimers, and $\Delta_j = 2\Delta$ for trimers, and $\Delta < 0$.

From these partition functions, $A_j = -kT \ln Q_j$, and $\Delta S = -\left(\frac{\partial \Delta A}{\partial T}\right)_{a,N}$, one can find general expressions for the measured thermodynamic quantities $\Delta G°$, $\Delta H°$, and $\Delta S°$ for dimer and trimer formation. For dimer formation, these are

https://doi.org/10.1021/acs.jpcb.3c04529
J. Phys. Chem. B 2024, 128, 603−621

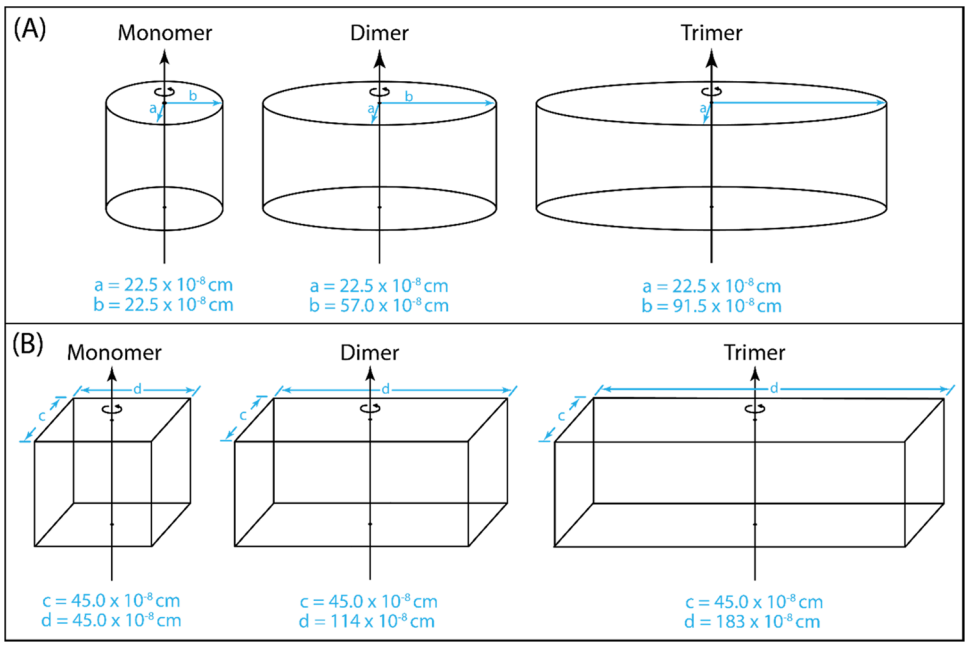

Figure 12. Rotational models for monomers, dimers, and trimers. (A) Solid elliptical cylinder rotational model. The black arrow indicates the principal rotational axis of the cylinder perpendicular to the plane of the membrane, and the blue arrows a and b are the short and long radii, respectively. (B) Solid cuboid rotational model. The black arrow indicates the principal rotational axis perpendicular to the plane of the membrane, and the blue arrows c and d indicate the width and length of the cuboid, respectively.

Table 3. Parameters for Statistical Mechanical Models

	3(AQPM1) ⇌ $(AQPM1)_2$ + (AQPM1) ⇌ $(AQPM1)_3$			
model	I (kg m^2)	θ_{rot} (K)	λ (cm^{-2} K^{-1})*	Δ (J)**
monomer (elliptical cylinder)	5.80×10^{-40}	6.96×10^{-7}	4.52×10^{18}	0
dimer (elliptical cylinder)	4.30×10^{-39}	9.38×10^{-8}	4.52×10^{18}	-1.57×10^{-19}
trimer (elliptical cylinder)	1.52×10^{-38}	2.64×10^{-8}	4.52×10^{18}	-1.57×10^{-19}
monomer (cuboid)	7.73×10^{-40}	5.22×10^{-7}	4.52×10^{18}	0
dimer (cuboid)	5.73×10^{-39}	7.03×10^{-8}	4.52×10^{18}	-1.57×10^{-19}
trimer (cuboid)	2.30×10^{-38}	1.98×10^{-8}	4.52×10^{18}	-1.57×10^{-19}
monomer (no rotations)			4.52×10^{18}	0
dimer (no rotations)			4.52×10^{18}	-1.59×10^{-19}
trimer (no rotations)			4.52×10^{18}	-1.59×10^{-19}

*$\lambda_{monomer} = \lambda$, $\lambda_{dimer} = 2\lambda$, and $\lambda_{trimer} = 3\lambda$, **$\Delta_{dimer} = \Delta$ and $\Delta_{trimer} = 2\Delta$.

$$\Delta G^{\circ}_{dimer} = -RT \ln\left(\frac{(2\lambda T)\left(\frac{T}{\theta_{rot,dimer}}\right)^{1/2} e^{-\Delta/kT}}{(\lambda T)^2\left(\frac{T}{\theta_{rot,monomer}}\right)} \times \theta^{\circ}\right) \quad (18)$$

$$\Delta S^{\circ}_{dimer} = R \ln\left(\frac{(2\lambda T)\left(\frac{T}{\theta_{rot,dimer}}\right)^{1/2}}{(\lambda T)^2\left(\frac{T}{\theta_{rot,monomer}}\right)} \times \theta^{\circ}\right) - \frac{5}{2}R \quad (19)$$

$$\Delta H^{\circ}_{dimer} = N_A\Delta - \frac{5}{2}RT \quad (20)$$

where R is the ideal gas constant and N_A is Avogadro's number. Note that the entire derivation is found in the Supporting Information accompanying this article.

For dimer formation (M1P and M1R), the moments of inertia for rotation around the principal axis perpendicular to the membrane were estimated by approximating both the monomer and dimer as either a solid elliptical cylinder or a solid cuboid. Figure 12 depicts the different rotational models for monomers, dimers, and trimers. The equation for the moment of inertia of an elliptical cylinder is,

$$I_{elliptical\ cylinder} = \frac{1}{4}m(a^2 + b^2) \quad (21)$$

where m is the mass, a is the radius along the short axis, and b is the radius along the long axis (see Figure 12A). The equation for the moment of inertia of a cuboid is

$$I_{cuboid} = \frac{1}{12}m(c^2 + d^2) \quad (22)$$

where c is the distance along the short face and d is the distance along the long face of the cuboid (see Figure 12B). Given that the mass of the monomer is 137.87 kg mol^{-1} and assuming that the dimensions of the monomers and dimers are similar to that measured for AQP4-M23,[26] the rotational temperatures and λ were calculated, using eqs 15 and 17, for both rotational models (as reported in Table 3). The

https://doi.org/10.1021/acs.jpcb.3c04529
J. Phys. Chem. B 2024, 128, 603−621

interaction potential was taken to be $\Delta = \frac{\Delta H^{\circ}_{\text{dimer}}}{N_A} + \frac{5}{2}kT$, where $\Delta H^{\circ}_{\text{dimer}} \sim -101$ kJ mol^{-1} (average between that measured for M1P and M1D). Then, at 298.15 K, $\Delta = -1.58 \times 10^{-19}$ J. Recalling that the standard state number density is taken to be $\theta^{\circ} = -2.10 \times 10^{12}$ cm^{-2}, the thermodynamics driving forces for dimer formation are estimated to be $\Delta G^{\circ}_{\text{dimer}} \sim 23$ kJ mol^{-1} and $\Delta S^{\circ}_{\text{dimer}} \sim 0.26$ kJ mol^{-1} for both rotational models ($\Delta H^{\circ}_{\text{dimer}}$ was taken from experiment). These results are included in Table 1 and are good approximations of the experimental values, giving strong evidence that the experimental observations are the result of dimer formation.

In a similar manner, the statistical mechanical relationships, ΔG°, ΔH°, and ΔS°, for trimer formation are

$$\Delta G^{\circ}_{\text{trimer}} = -RT \ln\left(\frac{(3\lambda T)\left(\frac{T}{\theta_{\text{rot,trimer}}}\right)^{1/2} e^{-2\Delta/kT}}{(\lambda T)^3\left(\frac{T}{\theta_{\text{rot,monomer}}}\right)^{3/2}} \times (\theta^{\circ})^2\right) \tag{23}$$

$$\Delta S^{\circ}_{\text{trimer}} = R \ln\left(\frac{(3\lambda T)\left(\frac{T}{\theta_{\text{rot,trimer}}}\right)^{1/2}}{(\lambda T)^3\left(\frac{T}{\theta_{\text{rot,monomer}}}\right)^{3/2}} \times (\theta^{\circ})^2\right) - 5R \tag{24}$$

$$\Delta H^{\circ}_{\text{trimer}} = 2N_A\Delta - 5RT \tag{25}$$

where the rotational temperatures are calculated using eqs 17, 21, and 22 for both the elliptical cylinder and cuboid moments of inertia. If we assume that the interaction potential is the same as above, $\Delta = -1.57 \times 10^{-19}$ J (the value used for the dimer interaction), then $\Delta H^{\circ}_{\text{trimer}} = -201$ kJ mol^{-1}, which is a close approximation to the experimental value. The theoretical value for Gibbs free energy for trimer formation is $\Delta G^{\circ}_{\text{trimer}} \sim -45.3$ kJ mol^{-1}, which is in approximate agreement with the measured value (-56.2 kJ mol^{-1}). Likewise, the theoretical value for the change in entropy for trimer formation is $\Delta S^{\circ}_{\text{trimer}} \sim -0.522$ kJ mol^{-1} K^{-1} in good agreement with experiment (-0.429 kJ mol^{-1} K^{-1}). This gives additional confidence in the interpretation of the experimental data.

4.5. Importance of the Rotational Degrees of Freedom. The contribution of the rotational degree of freedom to the overall thermodynamic driving forces is significant. To explore this in more detail, the statistical thermodynamic relationships without the contributions of rotations (removing the $\left(\frac{T}{\theta_{j,\text{rot}}}\right)^{1/2}$ terms) were used to determine theoretical values. For dimer formation,

$$\Delta G^{\circ}_{\text{dimer,no rotations}} = -RT \ln\left(\frac{(2\lambda T)e^{-\Delta/kT}}{(\lambda T)^2} \times \theta^{\circ}\right) \tag{26}$$

$$\Delta S^{\circ}_{\text{dimer,no rotations}} = R \ln\left(\frac{(2\lambda T)}{(\lambda T)^2} \times \theta^{\circ}\right) - 2R \tag{27}$$

$$\Delta H^{\circ}_{\text{dimer,no rotations}} = N_A\Delta - 2RT \tag{28}$$

If we assume that the interaction potential is the same as above, $\Delta = -1.59 \times 10^{-19}$ J, then $\Delta H^{\circ}_{\text{dimer, no rotations}} = -100.55$ kJ mol^{-1}, which is nearly identical to the experimental value. Therefore, any change to ΔG° will be entropic in nature. As expected, the result of excluding rotations results in ΔS being much lower than experimental values, and $T^*\Delta S^{\circ}_{\text{dimer, no rotations}} = -53$ kJ mol^{-1} vs $T^*\Delta S^{\circ}_{\text{dimer, experimental}} = -69$ kJ mol^{-1} at 298.15 K. Likewise, the change in Gibbs free energy of formation is much larger than that observed from experiment, $\Delta G^{\circ}_{\text{dimer, no rotations}} = -47$ kJ mol^{-1} vs $\Delta G^{\circ}_{\text{dimer, no rotations}} = -27$ kJ mol^{-1}.

Finally, similar results are observed for trimer formation as well. The statistical thermodynamic relationships without contributions from rotations are given below:

$$\Delta G^{\circ}_{\text{trimer}} = -RT \ln\left(\frac{(3\lambda T)e^{-2\Delta/kT}}{(\lambda T)^3} \times (\theta^{\circ})^2\right) \tag{29}$$

$$\Delta S^{\circ}_{\text{trimer}} = R \ln\left(\frac{(3\lambda T)}{(\lambda T)^3} \times (\theta^{\circ})^2\right) - 4R \tag{30}$$

$$\Delta H^{\circ}_{\text{trimer}} = 2N_A\Delta - 4RT \tag{31}$$

and the change in enthalpy was calculated from eq 25, assuming $\Delta = -1.59 \times 10^{-19}$ J to give $\Delta H^{\circ}_{\text{trimer}} = -201.1$ kJ mol^{-1}. This is in approximate agreement with the experimentally determined value. The calculated value for the entropy of trimer formation is also much smaller than experimental values; $T^*\Delta S^{\circ}_{\text{trimer, no rotations}} = -108$ kJ mol^{-1} vs $T^*\Delta S^{\circ}_{\text{trimer, experimental}} = -128$ kJ mol^{-1} at 298.15 K. Finally, the Gibbs free energy of formation is much larger when rotations are ignored; $\Delta G^{\circ}_{\text{trimer, no rotations}} = -93.4$ kJ mol^{-1} vs $\Delta G^{\circ}_{\text{trimer, experimental}} = -56.2$ kJ mol^{-1}.

4.6. Relevance of AQP4 Aggregation in the Biological Context. The elucidation of the aggregation mechanisms exhibited by AQP4-M1 and AQP4-M23 is imperative for a comprehensive understanding of their respective and distinct roles in the physiological and physio-pathological astrocyte processes. This work describes fundamental chemical forces that drive aggregation between AQP4-M1s, but the interaction interfaces suggested in this study also exist in AQP-M23s and, therefore, give insight into the driving forces for OAP formation as well. Moreover, the experimental work led to a simple statistical mechanical model that can be applied to OAP formation and heterogeneous aggregation between the different AQP4 isoforms.

Importantly, AQP4-M1 has been correlated with enhancing cell migration,[52] a pivotal mechanism governing tissue development and repair. On the other hand, AQP4-M23 has been associated with prominent cell adhesion.[52,53] The overexpression or dysregulation of AQP4-M1 may promote aberrant cell migration, leading to invasive behavior and metastasis.[54,55] Conversely, AQP4-M23 has been associated with apoptosis, a programmed cell death process.[54] Dysregulated apoptosis is a common feature of various pathological conditions, including neurodegenerative diseases.[56] Understanding the specific mechanisms through which AQP4-M23 influences apoptosis can shed light on potential therapeutic strategies for diseases characterized by excessive cell death.

Contrary to its conventional perception as a mere conduit for water within the brain, recent evidence indicates that AQP4 assumes a more pivotal role in intricately shaping astrocytes behavior.[57,58] Interestingly, AQP4 has been recognized for its capacity to modulate cellular functions without directly influencing the numerical abundance of water channels or

https://doi.org/10.1021/acs.jpcb.3c04529
J. Phys. Chem. B 2024, 128, 603−621

the overall permeability of the cell. Instead, it exerts its regulatory influence by manipulating its aggregation state.

This evolving understanding underscores the need for a more detailed exploration of AQP4 structures and dynamics, extending beyond its conventional role in fluid homeostasis, for unraveling the complexities of normal physiological and pathological processes. Insights into these mechanisms could provide potential targets for therapeutic interventions aimed at promoting tissue regeneration and repair.

5. CONCLUSIONS

This is the first study to show that the AQP4-M1 isoform will form stable dimers and trimers. It is also the first study to show that the distribution of monomers, dimers, and trimers is highly dependent upon the palmitoylation state of the cysteines on the N-terminal tail and is temperature-dependent. Importantly, when palymitoylated, AQP4-M1 will only form dimers and is driven by an exothermic reaction that overcomes a loss in entropy to give a negative overall free energy change ($\Delta G^{\circ}_{M1P} = -28.0$ kJ mol^{-1} and $\Delta G^{\circ}_{M1R} = -27.7$ kJ mol^{-1}). In contrast, AQP4-M1 will only form trimers if it is depalmitoylated. The formation of trimers in M1D samples gives thermodynamic values approximately twice that of dimer formation in M1D and M1R samples. This was mostly attributed to the fact that two interfacial interactions are present in trimers and only one in dimers. These results indicate that the mechanism for trimer formation proceeds through a dimer intermediate. Through structure prediction, it is most likely that the dimers are held together through hydrogen-bond formation between two sets of R108−Y250 residues on adjacent AQP4 monomers and the trimers are held together with an additional two sets of hydrogen bonds between R108−Y250 residues on a third AQP4-M1 opposite the first interface. It was also shown that chemical depalmitoylation followed by chemical repalmitoylation results in a complete recovery of the mobility and thermodynamic properties of unmodified samples, providing a new method to study the palmitoylation states in these important membrane proteins. In addition to the experimental studies, a simple statistical mechanical model was developed to test the reasonableness of the experimental results. This model treated AQP4-M1s as a two-dimensional gas with an interaction potential holding the dimers and trimers together. The results of the theoretical modeling were in good agreement with experimental findings and gave further evidence to the validity that AQP4-M1 will form stable dimers and trimers. Finally, it was shown that the rotational degrees of freedom were an important inclusion to the model and that they could be successfully approximated using either a solid elliptical cylinder or cuboid rotating perpendicular to the membrane.

■ ASSOCIATED CONTENT

Supporting Information

The Supporting Information is available free of charge at https://pubs.acs.org/doi/10.1021/acs.jpcb.3c04529.

SDS-PAGE gels of purified M1P, M1D, and M1R; Western blot of purified AQP4-M1; FRAP analysis of Triton X-100 treated solid-supported cushioned bilayer membranes; statistical thermodynamic expression for dimer formation; statistical thermodynamic expression for trimer formation; and effects of including inter-AQP4-M1 aggregate vibrational modes (PDF)

Palmitoylated M1P movie (AVI)

Depalmitoylated M1D movie (AVI)

Repalmitoylated M1R movie (AVI)

■ AUTHOR INFORMATION

Corresponding Authors

Grazia Paola Nicchia − *Department of Bioscience, Biotechnologies and Environment, University of Bari Aldo Moro, Bari 70124, Italy; Dominick P. Purpura Department of Neuroscience, Albert Einstein College of Medicine, Bronx, New York 10461, United States;* Email: graziapaola.nicchia@uniba.it

James A. Brozik − *Department of Chemistry, Washington State University, Pullman, Washington 99164-4630, United States; Materials Science & Engineering Program, Washington State University, Pullman, Washington 99163-2711, United States;* orcid.org/0000-0003-2097-5051; Email: brozik@wsu.edu

Authors

Jessica D. Carder − *Department of Chemistry, Washington State University, Pullman, Washington 99164-4630, United States;* orcid.org/0000-0002-2194-3169

Barbara Barile − *Department of Bioscience, Biotechnologies and Environment, University of Bari Aldo Moro, Bari 70124, Italy;* orcid.org/0000-0002-5093-6662

Krista A. Shisler − *Department of Chemistry, Washington State University, Pullman, Washington 99164-4630, United States*

Francesco Pisani − *Department of Bioscience, Biotechnologies and Environment, University of Bari Aldo Moro, Bari 70124, Italy*

Antonio Frigeri − *Department of Translational Medicine and Neuroscience, University of Bari Aldo Moro, Bari 70124, Italy; Dominick P. Purpura Department of Neuroscience, Albert Einstein College of Medicine, Bronx, New York 10461, United States*

K. W. Hipps − *Department of Chemistry, Washington State University, Pullman, Washington 99164-4630, United States; Materials Science & Engineering Program, Washington State University, Pullman, Washington 99163-2711, United States;* orcid.org/0000-0002-5944-5114

Complete contact information is available at: https://pubs.acs.org/10.1021/acs.jpcb.3c04529

Author Contributions

The manuscript was written through the contributions of all authors. All authors have given approval to the final version of the manuscript.

Notes

The authors declare no competing financial interest.

■ ACKNOWLEDGMENTS

The authors thank Eric Jacobo for his generosity in volunteering his time to help revise this manuscript. This work was supported by the Air Force Office of Scientific Research FA9550-18-1-0344 (J.A.B. and G.P.N), FA9550-18-1-0395 (J.A.B.). G.P.N. and A.F. acknowledge the following Italian funding agencies: (1) NEXTGENERATIONEU (NGEU) funded by the Ministry of University and Research (MUR), (2) National Recovery and Resilience Plan (NRRP), (3) project MNESYS (DD no. 1553, 11.10.2022)

(PE0000006), and (4) National Center for Gene Therapy and Drugs based on RNA Technology (DD no. 1035, 17.06.2022) project CN00000041.

■ ABBREVIATIONS

AQP4 =aquaporin-4
AQP4-M23 =short form AQP4
AQP4-M1 =long for AQP4
M1P =naturally palmitoylated AQP4-M1
M1D =chemically depalmitoylated AQP4-M1
M1R =chemically repalmitoylated AQP4-M1
HAM =hydroxyl amine
NEM =*N*-ethylmalemide
DOL =degree of labeling
DOP =degree of palmitoylation
POPC =1-palmitoyl-2-oleoyl-glycerol-3-phosphocholine
PEG−PE =1,2-stearoyl-*sn*-glycerol-3-phosphoethanolamine-*N*-[methoxy(polyethylene glycol)-2000]
SUV =small unilamellar liposomes
TIRF =total internal reflection fluorescence

■ REFERENCES

(1) Saadoun, S.; Papadopoulos, M. C. Aquaporin-4 in brain and spinal cord oedema. *Neuroscience* **2010**, *168* (4), 1036−1046.
(2) Mader, S.; Brimberg, L. Aquaporin-4 Water Channel in the Brain and Its Implication for Health and Disease. *Cells* **2019**, *8* (2), 90.
(3) Salman, M. M.; Kitchen, P.; Halsey, A.; Wang, M. X.; Tornroth-Horsefield, S.; Conner, A. C.; Badaut, J.; Iliff, J. J.; Bill, R. M. Emerging roles for dynamic aquaporin-4 subcellular relocalization in CNS water homeostasis. *Brain* **2022**, *145* (1), 64−75.
(4) Graber, D. J.; Levy, M.; Kerr, D.; Wade, W. F. Neuromyelitis optica pathogenesis and aquaporin 4. *J. Neuroinflammation* **2008**, *5* (1), No. 22.
(5) Zamvil, S. S.; Slavin, A. J. Does MOG Ig-positive AQP4-seronegative opticospinal inflammatory disease justify a diagnosis of NMO spectrum disorder? *Neurol. Neuroimmunol. Neuroinflammation* **2015**, *2* (1), No. e62.
(6) Takahashi, T.; Fujihara, K.; Nakashima, I.; Misu, T.; Miyazawa, I.; Nakamura, M.; Watanabe, S.; Shiga, Y.; Kanaoka, C.; Fujimori, J.; et al. Anti-aquaporin-4 antibody is involved in the pathogenesis of NMO: a study on antibody titre. *Brain* **2007**, *130* (Pt 5), 1235−1243.
(7) Ho, J. D.; Yeh, R.; Sandstrom, A.; Chorny, I.; Harries, W. E. C.; Robbins, R. A.; Miercke, L. J. W.; Stroud, R. M. Crystal structure of human aquaporin 4 at 1.8 A and its mechanism of conductance. *Proc. Natl. Acad. Sci. U.S.A.* **2009**, *106* (18), 7437−7442.
(8) Palazzo, C.; Buccoliero, C.; Mola, M. G.; Abbrescia, P.; Nicchia, G. P.; Trojano, M.; Frigeri, A. AQP4ex is crucial for the anchoring of AQP4 at the astrocyte end-feet and for neuromyelitis optica antibody binding. *Acta Neuropathol. Commun.* **2019**, *7* (1), No. 51.
(9) De Bellis, M.; Pisani, F.; Mola, M. G.; Rosito, S.; Simone, L.; Buccoliero, C.; Trojano, M.; Nicchia, G. P.; Svelto, M.; Frigeri, A. Translational readthrough generates new astrocyte AQP4 isoforms that modulate supramolecular clustering, glial endfeet localization, and water transport. *Glia* **2017**, *65* (5), 790−803.
(10) Crane, J. M.; Van Hoek, A. N.; Skach, W. R.; Verkman, A. S. Aquaporin-4 dynamics in orthogonal arrays in live cells visualized by quantum dot single particle tracking. *Mol. Biol. Cell* **2008**, *19* (8), 3369−3378.
(11) Nagelhus, E. A.; Ottersen, O. P. Physiological roles of aquaporin-4 in brain. *Physiol. Rev.* **2013**, *93* (4), 1543−1562.
(12) Furman, C. S.; Gorelick-Feldman, D. A.; Davidson, K. G. V.; Yasumura, T.; Neely, J. D.; Agre, P.; Rash, J. E. Aquaporin-4 square array assembly: Opposing actions of M1 and M23 isoforms. *Proc. Natl. Acad. Sci. U.S.A.* **2003**, *100* (23), 13609−13614.
(13) Crane, J. M.; Verkman, A. S. Reversible, temperature-dependent supramolecular assembly of aquaporin-4 orthogonal arrays in live cell membranes. *Biophys. J.* **2009**, *97* (11), 3010−3018.
(14) Crane, J. M.; Verkman, A. S. Determinants of aquaporin-4 assembly in orthogonal arrays revealed by live-cell single-molecule fluorescence imaging. *J. Cell Sci.* **2009**, *122* (6), 813−821.
(15) Jin, B.-J.; Rossi, A.; Verkman, A. S. Model of Aquaporin-4 Supramolecular Assembly in Orthogonal Arrays Based on Heterotetrameric Association of M1-M23 Isoforms. *Biophys. J.* **2011**, *100* (12), 2936−2945.
(16) de Bellis, M.; Cibelli, A.; Mola, M. G.; Pisani, F.; Barile, B.; Mastrodonato, M.; Banitalebi, S.; Amiry-Moghaddam, M.; Abbrescia, P.; Frigeri, A.; et al. Orthogonal arrays of particle assembly are essential for normal aquaporin-4 expression level in the brain. *Glia* **2021**, *69* (2), 473−488.
(17) Nicchia, G. P.; Mastrototaro, M.; Rossi, A.; Pisani, F.; Tortorella, C.; Ruggieri, M.; Lia, A.; Trojano, M.; Frigeri, A.; Svelto, M. Aquaporin-4 orthogonal arrays of particles are the target for neuromyelitis optica autoantibodies. *Glia* **2009**, *57* (13), 1363−1373.
(18) Verkman, A. S.; Phuan, P.-W.; Asavapanumas, N.; Tradtrantip, L. Biology of AQP4 and Anti-AQP4 Antibody: Therapeutic Implications for NMO. *Brain Pathol.* **2013**, *23* (6), 684−695.
(19) Chum, T.; Glatzova, D.; Kvicalova, Z.; Malinsky, J.; Brdicka, T.; Cebecauer, M. The role of palmitoylation and transmembrane domain in sorting of transmembrane adaptor proteins. *J. Cell Sci.* **2016**, *129* (15), 3053.
(20) El-Husseini, A. E.; Craven, S. E.; Chetkovich, D. M.; Firestein, B. L.; Schnell, E.; Aoki, C.; Bredt, D. S. Dual palmitoylation of PSD-95 mediates its vesiculotubular sorting, postsynaptic targeting, and ion channel clustering. *J. Cell Biol.* **2000**, *148* (1), 159−172.
(21) Guan, X.; Fierke, C. A. Understanding Protein Palmitoylation: Biological Significance and Enzymology. *Sci. China: Chem.* **2011**, *54* (12), 1888−1897. From NLM PubMed-not-MEDLINE
(22) Chamberlain, L. H.; Shipston, M. J. The physiology of protein S-acylation. *Physiol. Rev.* **2015**, *95* (2), 341−376. From NLM Medline
(23) Greaves, J.; Prescott, G. R.; Gorleku, O. A.; Chamberlain, L. H. Regulation of SNAP-25 trafficking and function by palmitoylation. *Biochem. Soc. Trans.* **2010**, *38* (1), 163−166.
(24) Suzuki, H.; Nishikawa, K.; Hiroaki, Y.; Fujiyoshi, Y. Formation of aquaporin-4 arrays is inhibited by palmitoylation of N-terminal cysteine residues. *Biochim. Biophys. Acta, Biomembr.* **2008**, *1778* (4), 1181−1189.
(25) Roche, J.; Törnroth-Horsefield, S. Aquaporin Protein-Protein Interactions. *Int. J. Mol. Sci.* **2017**, *18* (11), 2255.
(26) Rash, J. E.; Davidson, K. G. V.; Yasumura, T.; Furman, C. S. Freeze-fracture and immunogold analysis of aquaporin-4 (AQP4) square arrays, with models of AQP4 lattice assembly. *Neuroscience* **2004**, *129* (4), 915−934.
(27) Höfinger, S.; Yamamoto, E.; Hirano, Y.; Zerbetto, F.; Narumi, T.; Yasuoka, K.; Yasui, M. Structural features of aquaporin 4 supporting the formation of arrays and junctions in biomembranes. *Biochim. Biophys. Acta, Biomembr.* **2012**, *1818* (9), 2234−2243.
(28) Rossi, A.; Pisani, F.; Nicchia, G. P.; Svelto, M.; Frigeri, A. Evidences for a leaky scanning mechanism for the synthesis of the shorter M23 protein isoform of aquaporin-4: implication in orthogonal array formation and neuromyelitis optica antibody interaction. *J. Biol. Chem.* **2010**, *285* (7), 4562−4569.
(29) Pisani, F.; Simone, L.; Mola, M.; De Bellis, M.; Mastrapasqua, M.; Ruggieri, M.; Trojano, M.; Nicchia, G.; Svelto, M.; Frigeri, A. Host-Cell Type Dependent Features of Recombinant Human Aquaporin-4 Orthogonal Arrays of Particles—New Insights for Structural and Functional Studies. *Cells* **2019**, *8* (2), 119.
(30) Drisdel, R. C.; Alexander, J. K.; Sayeed, A.; Green, W. N. Assays of protein palmitoylation. *Methods* **2006**, *40* (2), 127−134.
(31) ATTO-TEC. Thiol-Reactive ATTO-Label (Maleimides) 2021 https://www.atto-tec.com/images/ATTO/Procedures/Mal.pdf (accessed 2022 12−20−2022).
(32) Lam, K. T.; Taylor, E. L.; Thompson, A. J.; Ruepp, M. D.; Lochner, M.; Martinez, M. J.; Brozik, J. A. Direct Measurement of Single-Molecule Ligand−Receptor Interactions. *J. Phys. Chem. B* **2020**, *124* (36), 7791−7802.

https://doi.org/10.1021/acs.jpcb.3c04529
J. Phys. Chem. B 2024, 128, 603−621

(33) Martinez, M. J.; Carder, J. D.; Taylor, E. L.; Jacobo, E. P.; Kang, C.; Brozik, J. A. Thermodynamic Driving Forces of Redox-Dependent CPR Insertion into Biomimetic Endoplasmic Reticulum Membranes. *J. Phys. Chem. B* **2022**, *126*, 1691−1699.
(34) Barnaba, C.; Taylor, E.; Brozik, J. A. Dissociation Constants of Cytochrome P450 2C9/Cytochrome P450 Reductase Complexes in a Lipid Bilayer Membrane Depend on NADPH: A Single-Protein Tracking Study. *J. Am. Chem. Soc.* **2017**, *139* (49), 17923−17934.
(35) Barnaba, C.; Humphreys, S. C.; Barden, A. O.; Jones, J. P.; Brozik, J. A. Substrate Dependent Native Luminescence from Cytochromes P450 3A4, 2C9, and P450cam. *J. Phys. Chem. B* **2016**, *120* (12), 3038−3047.
(36) Barden, A. O. N. Measuring Membrane Mobility: A Comparison of Three Techniques Including Instrument and Method Development. Doctoral dissertation, Washington State University, 2014.
(37) Davis, R. W.; Flores, A.; Barrick, T. A.; Cox, J. M.; Brozik, S. M.; Lopez, G. P.; Brozik, J. A. Nanoporous microbead supported bilayers: stability, physical characterization, and incorporation of functional transmembrane proteins. *Langmuir* **2007**, *23* (7), 3864−3872.
(38) Dezi, M.; Di Cicco, A.; Bassereau, P.; Lévy, D. Detergent-mediated incorporation of transmembrane proteins in giant unilamellar vesicles with controlled physiological contents. *Proc. Natl. Acad. Sci. U.S.A.* **2013**, *110* (18), 7276−7281.
(39) Marx, D. C.; Fleming, K. G. Local Bilayer Hydrophobicity Modulates Membrane Protein Stability. *J. Am. Chem. Soc.* **2021**, *143* (2), 764−772.
(40) Crocker, J. C.; Grier, D. G. Methods of Digital Video Microscopy for Colloidal Studies. *J. Colloid Interface Sci.* **1996**, *179* (1), 298−310.
(41) Poudel, K. R.; Keller, D. J.; Brozik, J. A. Single Particle Tracking Reveals Corralling of a Transmembrane Protein in a Double-Cushioned Lipid Bilayer Assembly. *Langmuir* **2011**, *27* (1), 320−327. (acccessed 2021/06/30/18:33:45). From DOI.org (Crossref)
(42) Sternberg. Biomedical Image Processing. *Computer* **1983**, *16* (1), 22−34.
(43) Baek, M.; DiMaio, F.; Anishchenko, I.; Dauparas, J.; Ovchinnikov, S.; Lee, G. R.; Wang, J.; Cong, Q.; Kinch, L. N.; Schaeffer, R. D.; et al. Accurate prediction of protein structures and interactions using a three-track neural network. *Science* **2021**, *373* (6557), 871−876.
(44) Hiroaki, Y.; Tani, K.; Kamegawa, A.; Gyobu, N.; Nishikawa, K.; Suzuki, H.; Walz, T.; Sasaki, S.; Mitsuoka, K.; Kimura, K.; et al. Implications of the Aquaporin-4 Structure on Array Formation and Cell Adhesion. *J. Mol. Biol.* **2006**, *355* (4), 628−639.
(45) Matiello, M.; Schaefer-Klein, J. L.; Hebrink, D. D.; Kingsbury, D. J.; Atkinson, E. J.; Weinshenker, B. G. Genetic analysis of aquaporin-4 in neuromyelitis optica. *Neurology* **2011**, *77* (12), 1149.
(46) Sonnleitner, A.; Schütz, G. J.; Schmidt, T. Free Brownian Motion of Individual Lipid Molecules in Biomembranes. *Biophys. J.* **1999**, *77* (5), 2638−2642.
(47) Campbell, C. T.; Sprowl, L. H.; Árnadóttir, L. Equilibrium Constants and Rate Constants for Adsorbates: Two-Dimensional (2D) Ideal Gas, 2D Ideal Lattice Gas, and Ideal Hindered Translator Models. *J. Phys. Chem. C* **2016**, *120* (19), 10283−10297.
(48) Banyikwa, A. T.; Goos, A.; Kiemle, D. J.; Foulkes, M. A. C.; Braiman, M. S. Experimental and Computational Modeling of H-Bonded Arginine−Tyrosine Groupings in Aprotic Environments. *ACS Omega* **2017**, *2* (9), 5641−5659.
(49) Dragan, A. I.; Privalov, P. L. Unfolding of a Leucine zipper is not a Simple Two-state Transition. *J. Mol. Biol.* **2002**, *321* (5), 891−908.
(50) Creamer, T. P.; Rose, G. D. Interactions between hydrophobic side chains within alpha-helices. *Protein Sci.* **1995**, *4* (7), 1305−1314.
(51) Hartsough, D. S.; Merz, K. M., Jr. Protein dynamics and solvation in aqueous and nonaqueous environments. *J. Am. Chem. Soc.* **1993**, *115* (15), 6529−6537.
(52) Smith, A. J.; Jin, B.-J.; Ratelade, J.; Verkman, A. S. Aggregation state determines the localization and function of M1− and M23− aquaporin-4 in astrocytes. *J. Cell Biol.* **2014**, *204* (4), 559−573.
(53) Hiroaki, Y.; Tani, K.; Kamegawa, A.; Gyobu, N.; Nishikawa, K.; Suzuki, H.; Walz, T.; Sasaki, S.; Mitsuoka, K.; Kimura, K.; et al. Implications of the aquaporin-4 structure on array formation and cell adhesion. *J. Mol. Biol.* **2006**, *355* (4), 628−639.
(54) Simone, L.; Pisani, F.; Mola, M. G.; De Bellis, M.; Merla, G.; Micale, L.; Frigeri, A.; Vescovi, A. L.; Svelto, M.; Nicchia, G. P. AQP4 Aggregation State Is a Determinant for Glioma Cell Fate. *Cancer Res.* **2019**, *79* (9), 2182−2194. From NLM
(55) Lan, Y. L.; Wang, X.; Lou, J. C.; Ma, X. C.; Zhang, B. The potential roles of aquaporin 4 in malignant gliomas. *Oncotarget* **2017**, *8* (19), 32345−32355.
(56) Elmore, S. Apoptosis: a review of programmed cell death. *Toxicol. Pathol.* **2007**, *35* (4), 495−516.
(57) Jorgačevski, J.; Zorec, R.; Potokar, M. Insights into Cell Surface Expression, Supramolecular Organization, and Functions of Aquaporin 4 Isoforms in Astrocytes. *Cells* **2020**, *9* (12), 2622.
(58) Salman, M. M.; Kitchen, P.; Halsey, A.; Wang, M. X.; Törnroth-Horsefield, S.; Conner, A. C.; Badaut, J.; Iliff, J. J.; Bill, R. M. Emerging roles for dynamic aquaporin-4 subcellular relocalization in CNS water homeostasis. *Brain* **2022**, *145* (1), 64−75.

https://doi.org/10.1021/acs.jpcb.3c04529
J. Phys. Chem. B 2024, 128, 603−621